A reappraisal of the amorphization kinetics of water ice: Combined experimental and numerical investigations and amorphization cross-sections in the 90–120 K range

Audrey Moingeon, Eric Quirico, Olivier Poch, Mathilde Faure, P. Boduch, Alicja Domaracka, Hermann Rothard, B Schmitt, Marcel Toulemonde, Jimmy Rangama, et al.

Icarus 450 (2026) 116995

Contents lists available at ScienceDirect

Icarus

journal homepage: www.elsevier.com/locate/icarus

Research Paper

A reappraisal of the amorphization kinetics of water ice: Combined experimental and numerical investigations and amorphization cross-sections in the 90–120 K range

A. Moingeon [a,*], E. Quirico [a], O. Poch [a], M. Faure [a], P. Boduch [b], A. Domaracka [b], H. Rothard [b], B. Schmitt [a], M. Toulemonde [b,1], J. Rangama [b], D. Bockelée-Morvan [c], T. Fouchet [c], F. Leblanc [d], E. Lellouch [c], V. Zakharov [c]

[a] Univ. Grenoble Alpes, CNRS, IPAG, 38000 Grenoble, France
[b] Université Caen Normandie, ENSICAEN, CNRS, CEA, Normandie Univ, CIMAP UMR 6252, F-14000 Caen, France
[c] LIRA, Observatoire de Paris, Université PSL, CNRS, Sorbonne Université, Université Paris Cité, 5 place Jules Janssen, 92195 Meudon, France
[d] LATMOS, CNRS, Sorbonne Université, UVSQ, Paris, France

ARTICLE INFO

Keywords:
Ices, IR spectroscopy
Experimental techniques
Satellites, surfaces

ABSTRACT

Airless icy objects in the outer Solar System are continually exposed to energetic ion irradiation from the solar wind, solar energetic particles, galactic cosmic rays or magnetospheric particles in the case of the rings or satellites of the giant planets. This irradiation can induce the amorphization of crystalline water ice, a phenomenon observed on several icy objects. However, the kinetics of water ice amorphization remains poorly constrained at temperatures above 90 K, typical of Galilean satellites. To address this gap, new irradiation experiments were conducted using Mg, O and S ions with energies ranging from 36 to 126 keV at temperatures from 20 to 120 K. We demonstrate that the amorphization cross-section σ_{am} correlates with the electronic stopping power S_e, invalidating the assumption commonly made in previous studies that total stopping power (i.e. total dose) controls the water ice amorphization process. Our data also show that the amorphization cross-section decreases as the temperature increases from 20 to 120 K, and it depends on the ion flux. Numerical simulations using the inelastic thermal spike model fail to reproduce the evolution of the amorphization cross-section with temperature. The amorphization mechanism remains largely unknown. The inelastic interactions possibly involve the production of isolated defects, which eventually coalesce to form continuous amorphous domains. An irradiation-induced recrystallization process may explain the observed temperature dependency. Though the amorphization cross-sections do not correlate with the nuclear stopping power, the contribution of elastic interactions cannot be fully ruled out. However, the interplay between the two types of interactions, inelastic and elastic, remains elusive.

1. Introduction

Water ice is a key component of the surfaces of icy satellites orbiting giant planets, trans-Neptunian Objects, Trojan asteroids and comets (Davies et al., 1997; Dalton et al., 2010; Brown, 2016; Terai et al., 2016). The surfaces of these airless objects (at the exception of Titan and Triton for the icy satellites, and Pluto for the TNOs) are directly exposed to energetic ion processing: Solar Wind (SW), Solar Energetic Particles (SEPs), Galactic Cosmic Rays (GCRs) and magnetospheric particles in the case of icy satellites (Moore et al., 2007; Hudson et al., 2008; Loeffler et al., 2011; Ding et al., 2013; Rothard et al., 2017; Loeffler et al., 2020). Energetic ions generate sputtering (H_2O, O_2, H_2O_2, OH^+, $(H_2O)^+$, $(H_3O)^+$ and clusters like $(H_2O)_nH^+$ with n=1-8) (Bar-Nun et al., 1985; De Barros et al., 2011; Martinez et al., 2019), a weak radiolysis of water (mostly confined in the first tens of Å) (Teolis et al., 2017) and amorphization (Famá et al., 2010). All these processes must be studied and quantified in order to assess the chemical and structural evolution of the surface, as well as its interaction with the exosphere, in the case of large objects (Vorburger et al., 2022).

On Jovian satellites such as Europa and Ganymede, the main form of water ice is crystalline, but amorphous water ice has been detected (Hansen and McCord, 2004; Ligier et al., 2016, 2019; Bockelée-Morvan et al., 2024). The detection of amorphous water ice exclusively

* Corresponding author.
E-mail address: audrey.moingeon@univ-grenoble-alpes.fr (A. Moingeon).
[1] Retired.

https://doi.org/10.1016/j.icarus.2026.116995
Received 31 October 2025; Received in revised form 12 January 2026; Accepted 4 February 2026
Available online 14 February 2026

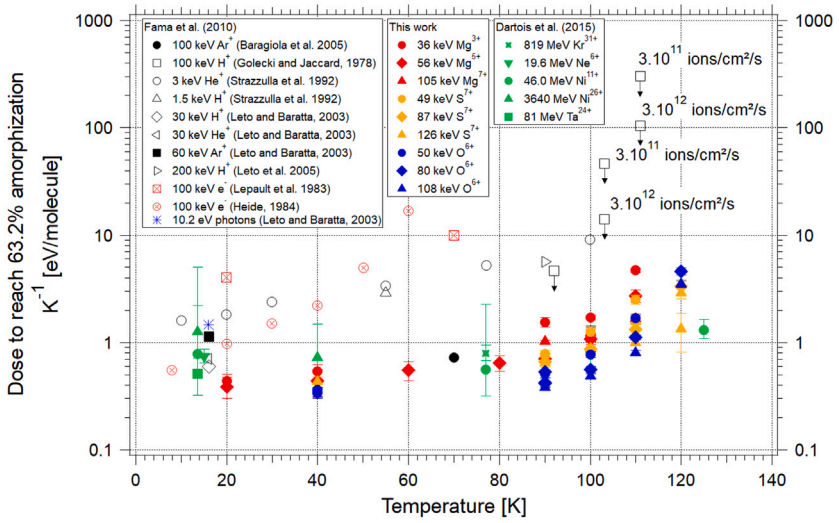

Fig. 1. Review of the published kinetic parameter K^{-1} of water ice amorphization. K^{-1} represents the total dose required to amorphize 63.2% of crystalline water ice (Eqs. (1) and (2)). The K^{-1} values determined in this study are presented as a function of temperature (filled symbols) for magnesium (red), sulfur (orange) and oxygen (blue) ions. For comparison, values from the review by Famá et al. (2010) (open symbols) and the experiments of Dartois et al. (2015) (green) are also included. Arrows indicate upper limits for values from Golecki and Jaccard (1978). Adapted from the review by Famá et al. (2010). (For interpretation of the references to color in this figure legend, the reader is referred to the web version of this article.)

in the polar regions of Ganymede by Bockelée-Morvan et al. (2024) is consistent with the expected physical conditions, as Ganymede's intrinsic magnetic field shields its equatorial regions from charged particle bombardment, resulting in higher irradiation at the poles (Kivelson et al., 1996; Fatemi et al., 2016; Poppe et al., 2018; Liuzzo et al., 2020; Plainaki et al., 2020; Paranicas et al., 2022), and the polar regions are cold enough to limit the extent of recrystallization. In order to simulate the effects of ion irradiation at the surface of these objects, knowledge about the kinetics of water ice amorphization is essential. Several experimental studies are reported in the literature, most of them at temperatures below 90 K (Golecki and Jaccard, 1978; Lepault et al., 1983; Heide, 1984; Strazzulla et al., 1992; Leto and Baratta, 2003; Leto et al., 2005; Baragiola et al., 2005; Famá et al., 2010; Dartois et al., 2015), which is under the temperature range of interest for Galilean icy satellites. All these studies are based on a kinetic equation relating the amorphous fraction Φ_A to the total dose deposited in the sample (see Appendix A for definitions of the various quantities used hereafter):

$$\Phi_A = \Phi_{A_{max}}(1 - e^{-KD}) \tag{1}$$

where $\Phi_{A_{max}}$ is the maximum value of the amorphous fraction, D is the total dose deposited in the ice and K is the kinetic parameter. The total dose D (eV/molecule) deposited in the film can be computed by:

$$D = (S_e + S_n)F\frac{M}{\rho N_a} \tag{2}$$

where S_e an S_n are the electronic and nuclear stopping powers (keV/μm), respectively, calculated with the SRIM software (Ziegler et al., 2010) and averaged on the film thickness. F is the fluence (ions.cm^{-2}), M is the molar mass and is equal to 18 g.mol^{-1}, ρ is the density and is equal to 0.93 g.cm^{-3} and $N_a = 6.022 \times 10^{23}$ mol^{-1} is the Avogadro number. K^{-1} (=$1/K$) represents the total dose required to amorphize 63.2% of crystalline water ice. All experiments, including ours presented in this study, with the exception of that of Strazzulla et al. (1992), obtained $\Phi_{A_{max}}$=1, meaning a complete amorphization at the end of the irradiation. The result of the study of Strazzulla et al. (1992) disagrees with the others because it likely suffered from a beam misalignment, precluding the amorphization of part of the sample.

The study by Famá et al. (2010) used this Eq. (1) to compute the kinetic evolution of amorphization and to compare sets of data collected by different experiments or laboratories. This latter publication compares the K^{-1} parameter from various studies mentioned above, which are presented on Fig. 1, together with the results from Dartois et al. (2015). Empty black symbols represent values derived from irradiations using low-energy ions (Golecki and Jaccard, 1978; Strazzulla et al., 1992; Leto and Baratta, 2003; Baragiola et al., 2005; Leto et al., 2005), whereas green points correspond to swift heavy ions irradiations (Dartois et al., 2015). The empty red points represent data obtained from electron irradiations, which do not lead to amorphization at temperatures above 70 K (Lepault et al., 1983; Heide, 1984). The blue star symbol corresponds to the K^{-1} value obtained from photon irradiation (Leto and Baratta, 2003).

This compilation shows that, above 90 K, the data points span a broad range of values, suggesting the role of other parameters and potential biases due to differences in the techniques used to quantify the amorphization yield and in the methods for analyzing the data. A second remark is that only two sets of data cover temperatures higher than 90 K (Golecki and Jaccard, 1978; Dartois et al., 2015), but employed very different conditions and analytical methods: 100 keV protons and Rutherford backscattering for the former; swift heavy ions and infrared spectroscopy for the latter. Golecki and Jaccard (1978) determined minimum crystallization yields, which means that their derived K^{-1} values can only be considered as upper limits. In addition, they report a flux dependence that needs to be determined.

The main goal of this study is to address the issues regarding the water ice amorphization depending on experimental parameters and to provide amorphization cross-sections over temperature and energy ranges of interest for the Jovian icy moons, typically between 90–160 K (Orton et al., 1996) and 10-10^7 eV (Poppe et al., 2018). Within this temperature range, the use of ions rather than electrons is more appropriate, as previous studies have demonstrated that electrons do not amorphize water ice (Lepault et al., 1983; Heide, 1984; Loeffler et al., 2020). Contrary to the kinetic coefficient K, which relies on the assumption that both the nuclear and electronic interactions control the amorphization process (see Eqs. (1) and (2)), the amorphization cross-section only relies on the experimental data with no a priori hypothesis. We have thus related the amorphous fraction Φ_A to the amorphization cross-section σ_{am}:

$$\Phi_A = \Phi_{A_{max}}(1 - e^{-\sigma_{am}F}) \tag{3}$$

where σ_{am} is expressed in cm^2/ion.

We present new results from irradiation experiments conducted with Mg, O and S ions at energies ranging from 36 to 126 keV and temperatures between 20 and 120 K. The ion masses and energies were selected to investigate a broad range of electronic and nuclear stopping powers. Particular attention was given to the 90–120 K temperature range, in order to best reproduce the conditions relevant to icy satellites such as Ganymede, while ensuring that recrystallization of amorphized water ice remained limited over the duration of the experiment. The obtained experimental amorphization cross-sections were extrapolated to a wider range of energies relevant for the Jovian icy moons at 90, 100 and 110 K, using the parametric equations of the analytical Thermal Spike model (hereafter a-TS) (Szenes, 1995). The ability of the numerical inelastic Thermal Spike model (hereafter i-TS) (Dufour et al., 1992; Toulemonde et al., 1992) to reproduce the experimental results was tested, and alternative models were also discussed. The paper is organized as follows: Section 2 describes the methodology employed to determine the amorphous fraction during irradiation and the amorphization cross-sections; results are presented in Section 3, and they are discussed in Section 4.

2. Experimental methods

Irradiation experiments were performed in July and October 2024 on the ARIBE beamline (“Accélérateur pour la Recherche avec les Ions de Basse Energie”: Accelerator for research with low-energy ions) at the Grand Accélérateur National d’Ions Lourds (GANIL, Caen, France).[2] O^{6+}, Mg^{3+}, Mg^{5+}, Mg^{7+} and S^{7+} ions between 36 and 126 keV were produced in the electron cyclotron resonance ion source and ion energies were obtained by combining the acceleration voltage and ion charge. We have used the IGLIAS setup (Augé et al., 2018) to synthesize thin ice films, irradiate them and monitor their structural evolution by infrared spectroscopy.

The ion beams were directed toward the IGLIAS experimental setup. To ensure uniform irradiation of the ice samples, a beam-sweeping device was employed (see Lv et al., 2012). This system consists of two pairs of parallel metallic plates that deflect the beam along both the horizontal and vertical directions. After sweeping, the ions passed through an insulated collimator with a circular aperture of 24 mm in diameter. A fraction of the beam was intercepted by the collimator, and the resulting collimator current was recorded. A Faraday cup could then be introduced into the beam path approximately 28.6 cm upstream from the target. By comparing the currents measured on the collimator and in the Faraday cup, the ion flux incident on the target (expressed as the number of projectiles per square centimeter per second) was determined. The total charge collected on the collimator was measured using ORTEC current integrators. Combining this accumulated charge with the ratio of the collimator current to the Faraday cup current allowed the projectile fluence (i.e., the total number of projectiles per square centimeter) to be calculated. This ratio was repeatedly verified throughout the experiment to ensure the stability of the beam flux.

Infrared spectra were collected using a Bruker 70v spectrometer, which was operated in the near- and mid-IR range (8000-550 cm^{-1}). The spectrometer was equipped with a MCT detector, a KBr beamsplitter, and a Globar source. The spectral resolution was set at 2 cm^{-1}, the apodization function was a Three-Term Blackman–Harris window, and a zero-filling factor of 2 was employed. Crystalline water ice films were obtained from the deposition at normal incidence of gaseous water on a ZnSe window at 150 K. They were likely polycrystalline, but the size of the crystallites could not be determined. The distance between the injection inlet and the window was 15 mm. Liquid water was filled in a stainless steel cylinder that was plugged on an ultravacuum line. Water was purified by subjecting it to three freeze-thaw cycles with liquid nitrogen. No interferometric system for measuring the film thickness during deposition was available, so the thicknesses of thin films were initially estimated after deposition from the maximum absorbance value of the broad 3250 cm^{-1} band of crystalline water ice, using the optical constants of Mastrapa et al. (2009) and Tegler et al. (2024). This step led to optimized values of deposition time and pressure in the chamber for controlling thickness, typically between 10 s and 1 min at 2×10^{-7} mbar. The film thickness was finally established to be less than half of the projectile’s penetration depth in the ice. This ensures that the electronic, nuclear and total stopping powers do not differ by more than 20% between the entrance and the exit of the sample due to the energy loss of the projectile ion. Furthermore, implantation of the projectiles in the thin ice film cannot occur. The projected range values were calculated with the SRIM software (Ziegler et al., 2010) and are provided in Table 1.

Subsequent to the process of deposition, the crystalline ice film was cooled to the desired irradiation temperature (20–120 K). It is important to note that, in this context, “crystalline water ice” refers to either the metastable cubic Ic or the hexagonal Ih crystalline forms of water ice. However, the precise crystalline nature of thin films remains uncertain due to the presence of stacking disorders during the film’s growth process. This uncertainty is influenced by a multitude of experimental parameters and infrared spectroscopy lacks the capability to differentiate between the Ic and Ih phases (Shilling et al., 2006; Salzmann et al., 2011; Kim et al., 2023).

The fraction of amorphous water ice in the ice film during irradiation was determined from infrared spectra collected every 30 s. The typical spectrum of crystalline water ice shows several vibration bands as (i) a libration band ν_L at ~ 980 cm^{-1}, due to a hindered rotation of the molecule in its crystallographic site; (ii) the ν_2 bending band at ~ 1650 cm^{-1}; (iii) the combination band $\nu_2 + \nu_L$ at 2230 cm^{-1} and (iv) the broad feature centered at ~ 3250 cm^{-1} (hereafter, the OH stretching band), which is controlled by the symmetric and antisymmetric vibration modes ν_1 and ν_3, respectively and contains three components: the Transverse Optic (TO) (A_1 symmetry) mode at 3120 cm^{-1}, the TO (E symmetry) mode at 3220 cm^{-1} and the Longitudinal Optic (LO) mode at 3380 cm^{-1} (Whalley, 1977). Each of these components involves both the ν_1 and ν_3 vibration modes, which are tightly coupled. The high spectral congestion of this band is due to the fact that crystalline water ice has an ordered lattice of oxygen atoms, either hexagonal for Ih or face centered-cubic for Ic, but hydrogen atoms are disordered and propagate through the lattice by tunneling (Drechsel-Grau and Marx, 2014). In contrast, in amorphous water ice the positions of O atoms are disordered and the OH stretching band appears as a broad unstructured feature (Fig. 2(a)). During irradiation, we observe the progressive transformation of the spectrum from crystalline to amorphous, as shown at 90 K in Fig. 2(a). Additional examples at temperatures ranging from 20 to 120 K are provided in Appendix B. Additional examples at temperatures ranging from 20 to 120 K are provided in Appendix B. In between, any spectrum is assumed to be represented by a linear combination of pure crystalline and amorphous water ice end-member spectra (Strazzulla et al., 1992; Famá et al., 2010):

$$S = \Phi_A S_a + (1 - \Phi_A) S_c \tag{4}$$

where S_c and S_a are, respectively, the spectra of fully crystalline and amorphous water ice, collected before and after the irradiation, respectively. The fit was computed with a Levenberg–Marquardt algorithm in the spectral range 2900 to 3700 cm^{-1}, after a baseline correction based on spline functions. The data analysis was performed with the software Igor Pro 8, Wavemetrics Inc. This approach enabled the estimation of the fraction of amorphous water ice Φ_A throughout the irradiation process. Sputtering is an issue in the case of high-energy experiments employing swift heavy ions (Dartois et al., 2015). In our case, we tried to estimate sputtering using the IR spectra by monitoring the decrease in the amplitude of the OH stretching band. Once this band no longer changed during irradiation, indicating that the sample is completely amorphized, irradiation continued in the expectation of observing a

[2] https://www.ganil-spiral2.eu/

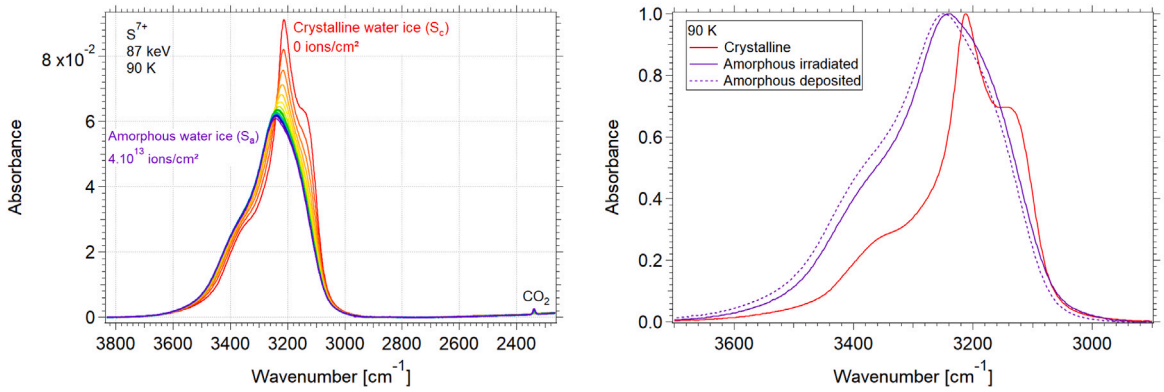

Fig. 2. *Left:* Spectra resulting from the irradiation of water ice with 87 keV S^{7+} ions at 90 K. The red crystalline and purple amorphous water ice spectra were used to compute the amorphous fraction throughout the irradiation using the linear combination (4). *Right:* Crystalline spectrum measured at 90 K, after deposition at 150 K and cooling down (red). Amorphous spectrum obtained after irradiation of a crystalline film with 87 keV S^{7+} ions at 90 K (solid purple). Amorphous spectrum formed by deposition at 50 K and measured at 90 K (dotted purple). All spectra are normalized at the wavelength of their maximum absorbance. (For interpretation of the references to color in this figure legend, the reader is referred to the web version of this article.)

decrease in the OH stretching band. However, this decrease was not significant enough to estimate sputtering in our case of low-energy experiments. Note that the linear assumption (Eq. (4)), though used in many earlier studies, has so far not been validated by combined Infrared and X-ray diffraction analyses. Finally, and very importantly, we have checked the alignment of the IGLIAS setup with the ARIBE ion beam, i.e. that the infrared beam section on the sample was totally overlapping the ion beam section. For that purpose, before each measurement campaign, we have deposited a thin layer of crystalline water ice, then cooled it at 16 K and irradiated it. The obtention of a spectrum of pure amorphous ice after irradiation confirmed the good alignment of the setup.

Finally, it should be noted that the spectrum of amorphous water ice formed from irradiation of crystalline water ice at a given temperature shows differences compared to an amorphous ice formed by deposition at 50 K and heated to the same temperature as the irradiated crystalline film (Fig. 2(b)). Such a dataset of deposited amorphous spectra was acquired during a previous experimental session in April 2024. Water ice films were deposited at 50 K and progressively heated to 160 K, with IR spectra collected every 10 K. The spectrum obtained at 90 K is shown in Fig. 2(b) and compared to that of an irradiated crystalline film at the same temperature. Notably, the deposited amorphous spectrum appears slightly shifted by 10.6 cm^{-1} with respect to the irradiated sample, as previously observed by Baratta et al. (1991). All spectra of amorphous water ice deposited at 50 K and warmed to 160 K are available on the SSHADE database infrastructure (Moingeon et al., 2024a). This point is of interest if these data are used for interpreting remote sensing data of satellites or Trans-Neptunian Objects for instance.

3. Results

3.1. Kinetics of water ice amorphization

All irradiation experiments performed in this study are summarized in Table 1. The K parameter in Eq. (1) was determined for each irradiation experiment by fitting the amorphous fraction Φ_A as a function of the dose following Eq. (1). Fig. 1 shows the K^{-1} values plotted as a function of temperature, along with data compiled in the review by Famá et al. (2010) and Dartois et al. (2015). In this figure, the lower is the K^{-1} value, the more effective is the amorphization. Two different trends can be distinguished above 90 K: the upper limits obtained from light ions (Golecki and Jaccard, 1978) are 2 to 3 orders of magnitude higher than the values obtained with swift heavy ions (Dartois et al., 2015).

Our experimental results are indicated in red (magnesium), orange (sulfur) and blue (oxygen). Uncertainties on the K^{-1} values were calculated from the fit uncertainty of intermediate spectra during amorphization when determining Φ_A with Eq. (4), and from the uncertainty of water ice density $\rho = 0.93 \pm 0.02$ g.cm^{-3}. This value corresponds to the density measured in water ice films deposited at temperatures above 120 K (Berland et al., 1995; Brown et al., 1996). However, the sample is compacted and amorphized during irradiation, which may lead to an increase of density. The type of resulting amorphous ice, and thus its density, remains undetermined. For simplicity, we assume that the sample density remains constant during irradiation in order to process the data. At temperatures above 90 K, our values span over slightly less than an order of magnitude, but are closer to the data of Dartois et al. (2015) than those of Golecki and Jaccard (1978). Below 90 K, they also match better with those from Dartois et al. (2015) than those from Strazzulla et al. (1992). An overall increase in K^{-1} with temperature is observed, in agreement with previous studies, suggesting a reduced efficiency of amorphization at higher temperatures.

3.2. Amorphization cross-section

According to Famá et al. (2010), the dispersion of the K^{-1} values obtained for similar temperatures by different experiments could be due to intrinsic differences of the experimental methods: Rutherford backscattering (Golecki and Jaccard, 1978), electron diffraction (Lepault et al., 1983; Heide, 1984) or IR spectroscopy (Strazzulla et al., 1992; Leto and Baratta, 2003; Baragiola et al., 2005; Leto et al., 2005). However, the K^{-1} values derived from our experiments at a given temperature show variability with the ion species, energies and charges, even though they have been collected with the same experimental set-up, experimentators and data analysis (Fig. 1).

The expression of the amorphous fraction as a function of the total dose (Eq. (1)) hypothesizes that both the nuclear and electronic interactions control the amorphization process. However, to understand how the amorphous fraction depends on the various experimental parameters, it seems more appropriate to express the amorphization cross-section as a function of the fluence (Eq. (3)) with no a priori hypothesis. Therefore, the amorphization cross-sections σ_{am} were determined from Eq. (3), as illustrated in Fig. 3 for the case of 87 keV S^{7+} ions. We investigated how σ_{am} correlates with the different experimental parameters as the ion energy and the electronic, nuclear and total stopping powers. The amorphization cross-section σ_{am} values for all irradiation experiments are summarized in Table 1, and plotted against the parameters mentioned above in Fig. 4, only at 90 K to exclude

Table 1
Summary of all the irradiation experiments performed and analyzed in the present study.

Date	Ion	E[a] [keV]	PR[b] [nm]	S_e[c]	S_n[d] [±10% keV/μm]	T[e] [±1 K]	Thick.[f] [nm]	Irr. time[g] [min]	Flux[h] [ions/cm²/s]	K^{-1}[i] [eV/molecule]	σ_{am}[j] [10^{-13}cm²]	R[k] [nm]
09-07-2024	Mg^{7+}	105	387	88	140	90	161 ± 0.2	7	1.7×10^{11}	0.76 ± 0.09	0.96 ± 0.11	1.75 ± 0.10
				85	144	100	190 ± 0.3	9	1.6×10^{11}	1.12 ± 0.08	0.66 ± 0.05	1.45 ± 0.05
				88	139	110	151 ± 0.2	22	1.2×10^{11}	1.67 ± 0.17	0.43 ± 0.04	1.18 ± 0.06
10-07-2024	Mg^{7+}	105	387	89	137	90	130 ± 0.2	44	2.3×10^{10}	1.03 ± 0.03	0.71 ± 0.02	1.50 ± 0.02
				89	137	100	131 ± 0.2	13	1.5×10^{11}	1.18 ± 0.16	0.61 ± 0.08	1.40 ± 0.09
				92	132	100	69 ± 0.1	11	1.8×10^{11}	1.23 ± 0.21	0.59 ± 0.10	1.37 ± 0.12
11-07-2024	Mg^{5+}	56	196	63	178	20	78 ± 0.1	4	2.3×10^{11}	0.38 ± 0.08	2.02 ± 0.45	2.54 ± 0.28
				63	179	40	81 ± 0.1	4	2.3×10^{11}	0.44 ± 0.12	1.77 ± 0.50	2.38 ± 0.34
				64	177	60	74 ± 0.1	5	2.5×10^{11}	0.55 ± 0.11	1.41 ± 0.28	2.12 ± 0.21
				63	179	80	82 ± 0.1	8	2.3×10^{11}	0.64 ± 0.11	1.21 ± 0.20	1.96 ± 0.16
				63	179	90	82 ± 0.1	8	1.7×10^{11}	0.70 ± 0.08	1.10 ± 0.13	1.88 ± 0.11
				62	182	100	97 ± 0.1	9	2.0×10^{11}	1.08 ± 0.12	0.73 ± 0.08	1.52 ± 0.08
				62	180	110	89 ± 0.1	13	3.7×10^{11}	2.73 ± 0.37	0.29 ± 0.03	0.95 ± 0.06
12-07-2024	Mg^{3+}	36	123	49	202	20	47 ± 0.1	8	9.6×10^{10}	0.44 ± 0.06	1.83 ± 0.27	2.41 ± 0.18
				48	203	40	55 ± 0.1	8	1.0×10^{11}	0.54 ± 0.08	1.49 ± 0.22	2.18 ± 0.16
				49	202	90	49 ± 0.1	6	4.0×10^{11}	1.54 ± 0.16	0.52 ± 0.05	1.29 ± 0.07
				48	203	100	53 ± 0.1	16	1.4×10^{11}	1.71 ± 0.09	0.47 ± 0.02	1.23 ± 0.03
				48	203	110	53 ± 0.1	38	1.7×10^{11}	4.69 ± 0.21	0.17 ± 0.007	0.74 ± 0.02
08-10-2024	S^{7+}	126	299	155	222	40	101 ± 0.2	10	4.0×10^{10}	0.43 ± 0.05	2.82 ± 0.32	2.99 ± 0.17
				153	225	90	118 ± 0.2	14	4.9×10^{10}	0.64 ± 0.04	1.89 ± 0.11	2.45 ± 0.07
				154	224	100	113 ± 0.2	15	3.6×10^{10}	0.88 ± 0.04	1.39 ± 0.06	2.10 ± 0.05
				154	223	110	108 ± 0.2	48	2.3×10^{10}	1.58 ± 0.06	0.76 ± 0.03	1.56 ± 0.03
				154	224	110	112 ± 0.2	8	8.0×10^{10}	1.00 ± 0.06	1.22 ± 0.07	1.97 ± 0.06
				154	224	120	115 ± 0.2	3	4.6×10^{11}	1.33 ± 0.52	0.91 ± 0.4	1.70 ± 0.34
				154	224	120	111 ± 0.2	16	1.0×10^{11}	2.88 ± 0.36	0.42 ± 0.05	1.16 ± 0.07
09-10-2024	S^{7+}	87	203	136	254	90	73 ± 0.1	12	5.8×10^{10}	0.66 ± 0.07	1.89 ± 0.20	2.45 ± 0.13
				139	250	100	56 ± 0.1	12	5.8×10^{10}	0.86 ± 0.07	1.45 ± 0.11	2.15 ± 0.08
				138	252	110	64 ± 0.1	19	5.7×10^{10}	1.32 ± 0.14	0.95 ± 0.10	1.74 ± 0.09
				139	250	120	58 ± 0.1	20	9.8×10^{10}	3.31 ± 0.49	0.38 ± 0.06	1.10 ± 0.08
		49	116	100	297	90	54 ± 0.1	14	5.0×10^{10}	0.78 ± 0.06	1.66 ± 0.13	2.30 ± 0.09
				103	294	100	44 ± 0.1	16	5.0×10^{10}	1.25 ± 0.11	1.02 ± 0.09	1.80 ± 0.08
				103	295	110	45 ± 0.1	26	5.0×10^{10}	2.52 ± 0.24	0.51 ± 0.05	1.27 ± 0.06
10-10-2024	O^{6+}	108	527	127	58	90	177 ± 0.3	11	6.5×10^{10}	0.38 ± 0.02	1.56 ± 0.10	2.23 ± 0.07
				125	60	100	214 ± 0.3	12	6.5×10^{10}	0.48 ± 0.03	1.23 ± 0.06	1.98 ± 0.05
				127	58	110	173 ± 0.3	18	6.5×10^{10}	0.80 ± 0.04	0.74 ± 0.04	1.54 ± 0.04
				126	58	120	184 ± 0.3	74	6.3×10^{10}	3.52 ± 0.24	0.17 ± 0.01	0.73 ± 0.02
		80	388	112	69	90	146 ± 0.2	64	1.2×10^{10}	0.53 ± 0.01	1.09 ± 0.02	1.87 ± 0.02
				112	69	90	144 ± 0.2	15	6.0×10^{10}	0.42 ± 0.02	1.39 ± 0.08	2.10 ± 0.06
				114	67	90	115 ± 0.2	16	8.3×10^{10}	0.42 ± 0.04	1.39 ± 0.14	2.10 ± 0.11
				112	69	100	146 ± 0.2	20	6.0×10^{10}	0.56 ± 0.04	1.05 ± 0.07	1.83 ± 0.06
				113	68	110	137 ± 0.2	29	6.0×10^{10}	1.12 ± 0.06	0.52 ± 0.03	1.29 ± 0.03
				112	69	120	147 ± 0.2	83	5.8×10^{10}	4.59 ± 0.34	0.13 ± 0.009	0.64 ± 0.02
11-10-2024	O^{6+}	50	238	95	86	40	84 ± 0.1	49	1.3×10^{10}	0.36 ± 0.02	1.60 ± 0.09	2.26 ± 0.06
				96	85	40	79 ± 0.1	17	3.2×10^{10}	0.34 ± 0.03	1.72 ± 0.15	2.34 ± 0.11
				94	87	40	96 ± 0.1	9	6.0×10^{10}	0.34 ± 0.04	1.71 ± 0.19	2.33 ± 0.13
				97	84	90	68 ± 0.1	16	6.3×10^{10}	0.51 ± 0.04	1.13 ± 0.10	1.90 ± 0.08
				94	87	100	99 ± 0.1	20	6.2×10^{10}	0.77 ± 0.05	0.76 ± 0.05	1.55 ± 0.05
				95	86	110	90 ± 0.1	29	6.2×10^{10}	1.68 ± 0.11	0.35 ± 0.02	1.05 ± 0.03

[a] Ion energy.
[b] Projected range of the ion, given by the SRIM software (Ziegler et al., 2010) for a density $\rho = 0.93 \pm 0.02$ g.cm^{-3}.
[c] Electronic stopping powers, given by SRIM, average value within the sample thickness.
[d] Nuclear stopping powers, given by SRIM, average value within the sample thickness.
[e] Irradiation temperature.
[f] Thickness of the sample, determined using optical constants from Tegler et al. (2024).
[g] Irradiation time required to reach complete amorphization.
[h] Average flux throughout the irradiation experiment.
[i] Parameter representing the kinetics of the amorphization process (Eq. (1)).
[j] Amorphization cross-section (Eq. (3)).
[k] Amorphous track radius, determined using $\sigma_{am} = \pi R^2$.

temperature-dependent effects. However, the results obtained at 100 K and 110 K give qualitatively similar figures. We observe a significant correlation only with the stopping power S_e (Fig. 4(d)), where linear fits provide coefficients of determination $r^2 = 0.71$; 0.83; 0.83 for 90; 100; 110 K, respectively. All σ_{am} values at temperatures between 20 and 120 K are plotted as a function of S_e on Fig. 5(a). In contrast, we found no correlation between σ_{am} and S_n (Fig. 4(c)), and a weak correlation between K^{-1} and S_e (Fig. 4(e)) where $r^2 = 0.43$; 0.45; 0.63 for 90; 100; 110 K, respectively.

3.3. Flux effect

Some of our irradiation experiments were conducted with different fluxes, all other experimental parameters being identical. The results of this flux dependency are presented in Fig. 6. They show that the greater the flux, the more effective the amorphization. No flux dependence is observed for O^{6+} ions at 40 K and for Mg^{7+} ions at 100 K within the error bars, and only a weak increase is observed for O^{6+} ions at 90 K. However, this effect becomes very significant with 126 keV S^{7+} ions

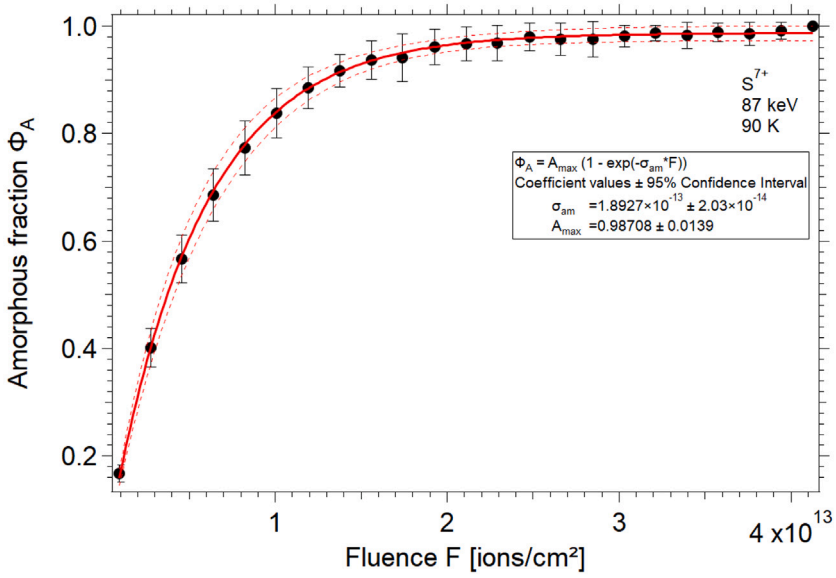

Fig. 3. Amorphous fraction as a function of fluence during irradiation with 87 keV S^{7+} ions. The data were fitted using Eq. (3) to determine the amorphization cross-section σ_{am}. The fit curve and associated parameters are given with 95% confidence intervals.

at 110 and 120 K, for which σ_{am} increases by a factor of 1.59 and 2.14, respectively. These results suggest that the dependence on ion flux is more significant at temperatures above 100 K. Due to the limited data available at different ion fluxes, we are unable to draw definitive conclusions regarding the influence of flux as a function of temperature.

A similar flux dependence was previously reported by Golecki and Jaccard (1978) at 102 and 111 K with 100 keV H^+ fluxes of 3×10^{11} and 3×10^{12} ions/cm^2/s. In this study, the amorphization yield was estimated from Rutherford backscattering experiments on oriented monocrystals along the c-axis and 9 ° off the c-axis. The fit of the first derivative of the minimum yield with an Arrhenius law provides two different ΔH values for the two fluxes. After ruling out the possibility of a simple thermal annealing, they came to the conclusion that the effect was governed by a radiation-assisted thermally-activated annealing. Radiation-assisted thermally activated annealing is a mechanism that consists of a recrystallization process catalyzed by irradiation. In that case, crystallization may occur at lower temperatures than those required for simple thermal activation. This empirical mechanism is described in analytical models using Arrhenius laws (e.g. Wang et al., 2000). A possible mechanism lies in the formation of clusters from charged interstitial species, thereby freeing channeling routes as observed in alkali solids (Hollis, 1973). Another or complementary interpretation is to invoke the slowing of the cooling rate through the repetitive addition of heat pulses from incoming ions, at a rate controlled by flux. This flux dependency questions the applicability of experimental simulations to planetary conditions, for which fluxes are lower by at least three orders of magnitude. Systematic dedicated experiments should be conducted in the future to solve this issue.

3.4. Thermal spike model

The physics of material modification induced by ion irradiation is far from being fully understood (Weber and Wendler, 2016; Zhang and Weber, 2020). In the case where electronic interactions dominate the process, several models have been developed, mostly in the case of refractory dielectrics, semi-conductors and metals: the two-temperature model (TTM), the inelastic thermal spike (i-TS) model, the Coulomb explosion model, the bond weakening model, or the self-trapped excitation model (Dufour and Toulemonde, 2016; Costantini and Ogawa, 2023 and references therein). To our knowledge, none were developed for hydrogen-bonded solids such as water ice. The thermal spike model developed by Szenes (1995) is based on a mechanism of local melting and rapid cooling that amorphizes the material through a quenching effect, occurring within a nanometric ion track. A numerical version of this model (i-TS) was subsequently developed and successfully applied to different types of materials (Dufour and Toulemonde, 2016). Famá et al. (2010) report that the thermal spike model accounts for the amorphization process of water ice. In this respect, we have conducted simulations with the i-TS model in order to reproduce our experimental results.

The thermal spike model was developed in the case of swift ions, for which interactions are dominated by the electronic regime (Szenes, 1995). It comprises, schematically, four distinct sequences (Dufour et al., 1993):

1. ionization and generation of a Coulomb field and primary electrons, confined in a ~ 1 nm large ion track;
2. electron–electron radial energy transfer, thermalization, and plasma formation;
3. electron–phonon energy transfer, leading to a temperature spike in the lattice confined in a cylindrical volume of ~ 10 nm;
4. cooling down, radiative decay, and several lattice processes.

The whole process is supposed to last between 10^{-17} and 10^{-11} s. If the amount of energy exceeds the latent fusion enthalpy, the material melts in the track and transforms into an amorphous phase due to the very fast cooling down.

Famá et al. (2010) used an analytical version of this model to interpret their own data and compiled data from the literature. In their study, the amorphization cross-section reads:

$$\sigma_{am} = \frac{g(S_e + S_n)}{\rho c (T_m - T_0)} \tag{5}$$

where $g < 1$ is the fraction of energy deposited in the sample, ρ is the density, c is the heat capacity, T_0 the initial temperature of the sample and T_m is the melting temperature. According to this equation, σ_{am} increases when T_0 increases if all parameters are independent of temperature, which contradicts the experimental results. According to the authors, using a temperature-dependent heat capacity would improve the model, leading to temperature dependence in line with

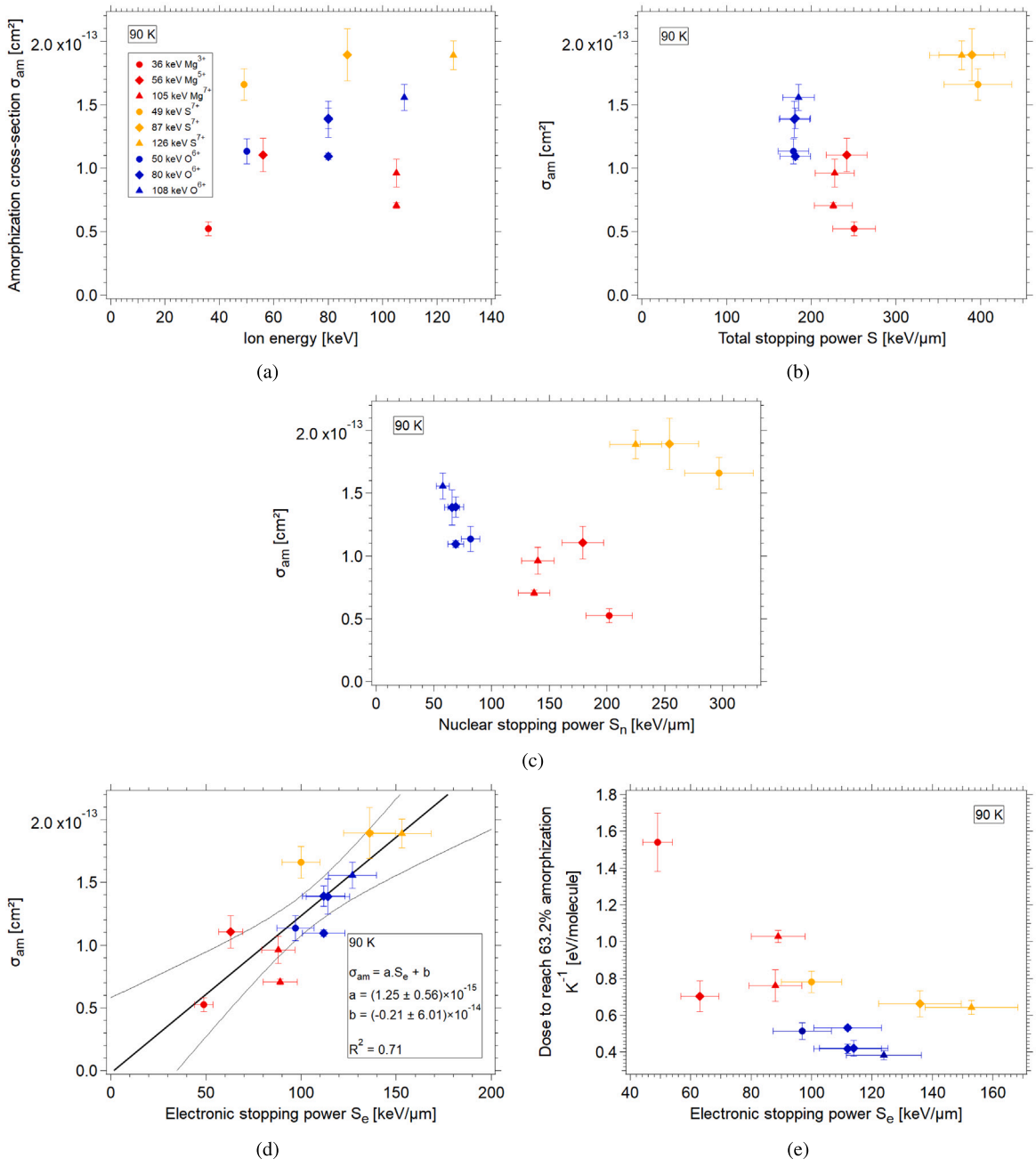

Fig. 4. Amorphization cross-section σ_{am} at 90 K as a function of (a) ion energy E, (b) total stopping power S, (c) nuclear stopping power S_n, (d) electronic stopping power S_e. A clear correlation is observed between σ_{am} and S_e as opposed to the other parameters. (e) K^{-1} values as a function of electronic stopping power S_e, derived from fitting the amorphous fraction Φ_A as a function of total dose D, with a 95% confidence interval. (For interpretation of the references to color in this figure legend, the reader is referred to the web version of this article.)

previous reports in the literature. However, no numerical model was employed to fit the measurements presented in their study. Another issue is the use of the total stopping power in Eq. (5), which does not distinguish between the respective contributions of S_e and S_n. According to our results, the contribution of S_e is more significant with respect to elastic interactions.

3.4.1. Numerical inelastic thermal spike model (i-TS)

To further explore these issues, we carried out numerical simulations using the i-TS numerical model (Dufour et al., 1992; Toulemonde et al., 1992). This model generated values of the radius R of the ion track, which were compared to experimental data. The experimental radius R was determined by assuming a Poisson distribution of the ions impacts. The probability that an impact happened at least one time, at a given location of the surface of the sample, can be written as $1 - \exp(-\pi R^2 F)$, where F is the fluence and $\pi R^2 F$ represents the average number of the impacts on a surface πR^2. The radius R can then be determined by Eq. (3) and leads to:

$$R^2 = \frac{\sigma_{am}}{\pi} \tag{6}$$

This equation only holds true under certain conditions: there must be no track overlap, no track coalescence and negligible structural relaxation.

The i-TS model has been developed to reproduce track formation in various materials, such as metals (Dunlop et al., 1994; Wang et al., 1994), insulators (Toulemonde et al., 2000; Meftah et al., 2005; Awazu

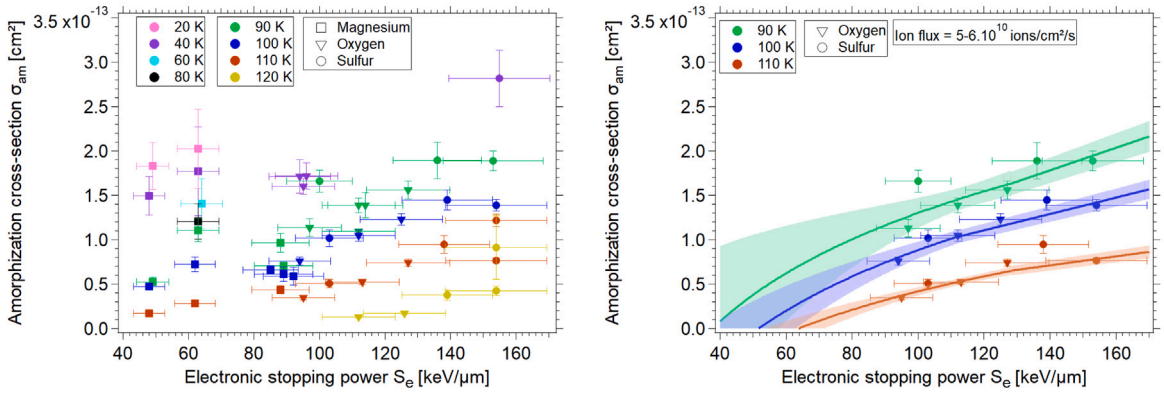

Fig. 5. *Left:* Amorphization cross-section σ_{am} as a function of electronic stopping power S_e, derived from fitting the amorphous fraction Φ_A as a function of fluence F, with a 95% confidence interval. *Right:* Part of the dataset presented in the left, collected with the same ion flux (5-6 × 10^{10} ions/cm^2/s) and fitted using Eqs. (11) and (12), with a 95% confidence interval.

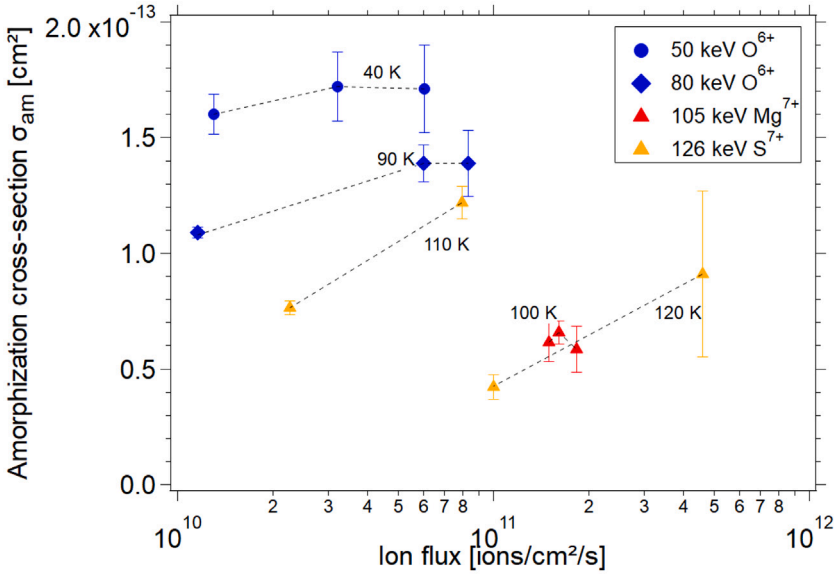

Fig. 6. Amorphization cross-section σ_{am} values as a function of ion flux. The lines are here to guide the eyes.

et al., 2006) and semi-conductors (Schnohr et al., 2010; Sall et al., 2015). It basically consists of two coupled equations of heat diffusion for electrons and atoms, at a distance r from the axis of a cylindrical ion track and at a time t:

$$C_e(T_e)\frac{\delta T_e}{\delta t} = \frac{1}{r}\frac{\delta}{\delta r}\left[rK_e(T_e)\frac{\delta T_e}{\delta r}\right] - g(T_e - T_a) + B(r,t) \quad (7)$$

$$C_a(T_a)\frac{\delta T_a}{\delta t} = \frac{1}{r}\frac{\delta}{\delta r}\left[rK_a(T_a)\frac{\delta T_a}{\delta r}\right] + g(T_e - T_a) \quad (8)$$

The parameters T_e, C_e, K_e and T_a, C_a, K_a represent the temperature, the specific heat (Toulemonde et al., 2009) and the thermal conductivity (Klinger, 1980) of the electrons and atoms of the system, respectively. $B(r,t)$ is the energy density per unit time deposited in the electronic system. The parameter g refers to the electron–phonon coupling. It is related to the electron–phonon mean free path λ through the equation $g = D_e C_e/\lambda^2$. For water, which has an energy band gap of 8.8 eV, the electronic parameter will be defined as for insulators (Toulemonde et al., 2000). In that case, the electron thermal diffusion is $D_e = 2$ cm^2/s and the electron specific heat $C_e = 1$ J/cm^3/K. Since neither g nor λ are known for water ice, λ is a free parameter in the fit of the experimental data.

The model numerically solves the coupled Eqs. (7) and (8) to obtain the evolution of T_e and T_a as a function of r and t. The temperature evolution of the lattice specific heat is the following: C_s(J/g/K) = $0.0076 \times T_a$ for T_a less than 273 K, equal to 4 between 273 K and 373 K and equal to 2 for T_a larger than 373 K (Handa and Klug, 1988). Additionally, the energy received by the water ice, E_i in eV/atom, is computed as a function of r and t based on the lattice temperature T_a:

$$E_i(T_a) = \frac{M}{3N_a 1.6\times10^{-19}}\int_0^{T_a} C_s dT,\ T_a < 273K \quad (9)$$

Due to the extremely rapid increase in temperature along the ion track, the transition between the solid and liquid phases does not occur at the melting temperature T_m, as observed with picosecond laser pulses (Hermes et al., 1986; Rethfeld et al., 2002). Consequently, the melting temperature (273 K for water ice) is no longer a suitable criterion, and a superheating scenario is applied. The latent heat L is added to the specific heat C_s in the computation of the deposited energy E_i, when $T_a > T_m$. Therefore, the energy to melt the material E_m is the following:

$$E_m(T_a) = \frac{M}{3N_a 1.6\times10^{-19}}\left(L + \int_0^{T_a} C_s dT\right) \quad (10)$$

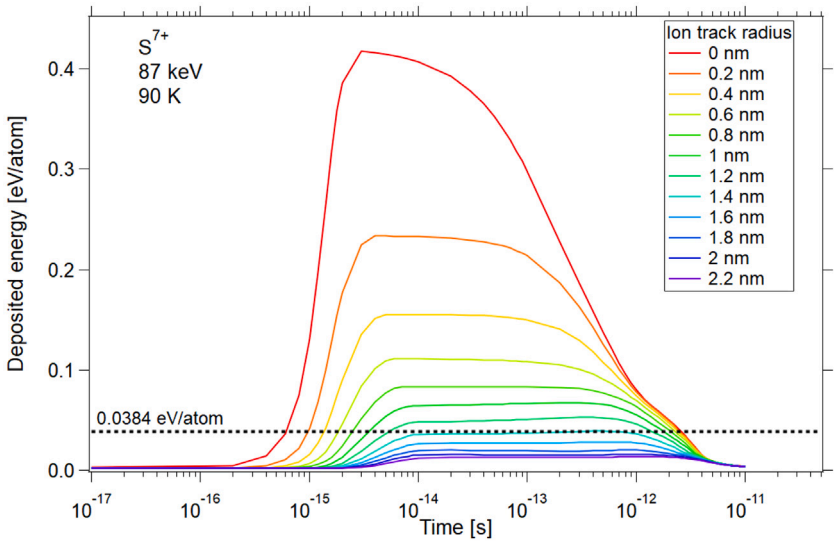

Fig. 7. Energy deposited in the ion track as a function of time, induced by ion irradiation in water ice, given by the i-TS model. 0.0384 eV/atom is the minimal energy deposited in the surface to melt the water ice, and transform it into an amorphous form.

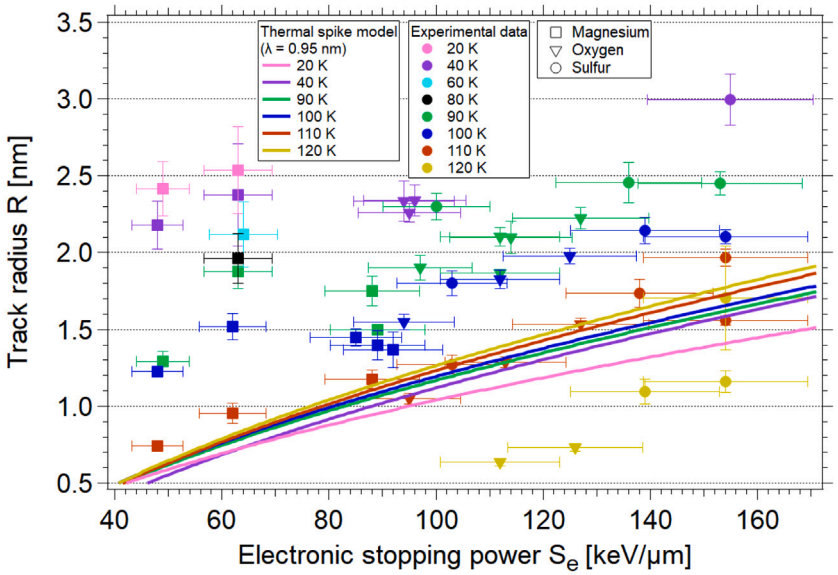

Fig. 8. Experimental track radius R (Eq. (6)) as a function of electronic stopping power S_e. The lines represent the values computed with the i-TS model, for λ = 0.95 nm. (For interpretation of the references to color in this figure legend, the reader is referred to the web version of this article.)

Fig. 7 illustrates the deposited energy as a function of time t for various radii r in water ice irradiated by 87 keV S^{7+} ions at 90 K. The ion track radius R is defined as the maximal radius at which the deposited energy exceeds the energy corresponding to the melting temperature of water, namely 0.0384 eV/atom. Following the peak temperature, the melted water ice cools down and recondenses within the track into an amorphous form due to the extremely rapid cooling process, occurring in less than 10^{-10} s, as shown in Fig. 7. Employing this method, modeled radii can be determined for each irradiation condition and different λ, and compared to the experimental track radius values.

R values for all our irradiation experiments are given in Table 1. Fig. 8 presents the experimental track radius R as a function of the electronic stopping power S_e. The colored lines represent the results obtained from the i-TS model, with the same irradiation conditions as our experiments. The value of λ was set to 0.95 nm to achieve the best possible fit to the experimental data at 110 K. Although the model could reproduce the evolution trend of experimental R values as a function of S_e, a major difference between our experimental data and the results given by i-TS model is the track radius dependence to the initial temperature T_0, as shown in Fig. 8. The model predicts a more efficient amorphization at higher temperatures, with higher R at 120 K (yellow curve) than at 40 K (purple curve). This is inconsistent with experimental results, which show that water ice amorphization is more efficient at lower temperatures. In the model, the track radius R is computed by calculating the energy required to heat the sample from T_0 to T_m. At a higher T_0 value, less energy is required to melt and the model predicts more efficient amorphization. This trend is observed in many cases for metallic materials (Dufour et al., 1999) and for insulator materials (Houpert et al., 1991), which have a much higher gap between T_0 and T_m than water ice in our experiment. One should note that water ice is a very different solid compared to those traditionally studied with the i-TS model. It is a molecular solid whose properties, controlled by inter-molecular hydrogen bonds and orientations, are highly temperature dependent (Franks, 1972), as suggested the paper of Mélot et al. (2003) for which the transformation of the

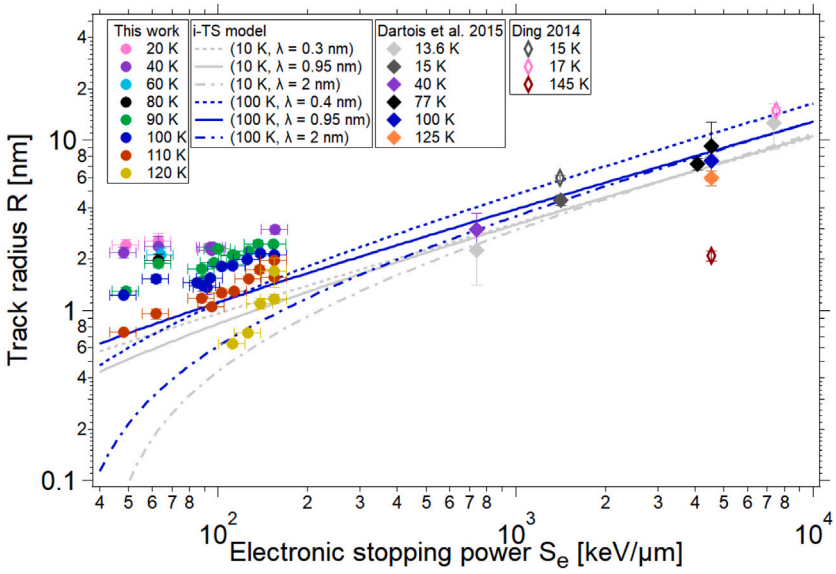

Fig. 9. Experimental track radius R (this work, Ding, 2014; Dartois et al., 2015) as a function of electronic stopping power S_e. Values computed with the i-TS model are included, using λ values between 0.3 and 2 nm.

material is larger under an irradiation at 8 K than for an irradiation at 290 K. Moreover, it has already been reported in the literature that the thermal spike model can describe the trend of the experimental data, but not their absolute values (Klaumünzer, 2006).

The only way to reproduce our inferred cross-section dependence to the temperature with this i-TS model may be to adjust the value of the λ parameter for each temperature. Fig. 9 presents numerical simulations with λ values ranging between 0.3 and 2 nm, compared with experimental data from literature (Ding, 2014; Dartois et al., 2015). This suggests that the water ice electron–phonon coupling g may increase (the electron–phonon mean free path λ may decrease) when the temperature decreases. However, the temperature dependence cannot be compensated by a varying λ, as illustrated in Fig. 9. The lower limit of λ was chosen based on computational capabilities, as a lower λ value requires smaller time steps and significantly longer calculation durations. The upper limit of $\lambda = 2$ nm is due to the fact that the model predicts $R = 0$ nm for S_e around 20 keV/µm, indicating no amorphization. However, the study by Strazzulla et al. (1992) demonstrated that water ice is amorphized with 1.5 keV H^+ and 3 keV He^+ ions, corresponding to $S_e \approx 17$ keV/µm. Therefore, a λ value greater than 2 nm would be inconsistent with experimental observations. At 10 K, the simulation curves for different λ are very close to each other for highest S_e (Fig. 9), and fit well the data of Dartois et al. (2015) at 13.6, 15 and 40 K. The data points of Ding (2014) at 15 and 17 K, and the data points at 20, 40 and 60 K of our study plot at higher R (Fig. 9). The simulation curves at 100 K correspond well to the data point at $S_e = 4556$ keV/µm from Dartois et al. (2015), for $0.95 < \lambda < 2$ nm. However, our data points at 100 K are not fitted, regardless of the λ value. Finally, using the only free parameter λ of the model does not reconcile the simulation curves and the experimental data in all cases, even considering a heat capacity depending on the temperature. The assertion posited by Famá et al. (2010) that a temperature-dependent heat capacity ensures the consistency of the thermal spike model appears to lack validity.

Last, simulations incorporating electronic and elastic interactions were conducted with the i-TS model (Fig. 10). The track radii were found to be systematically higher than the experimental values and not following the trend as a function of S_e, which means that this model does not explain the experimental results.

3.4.2. Analytical thermal spike model (a-TS)

In order to describe interactions between magnetospheric ions and the icy surfaces of Jovian satellites, we need to extrapolate the amorphization cross-section σ_{am} to a wider range of S_e values. Since the i-TS model does not reproduce our experimental data, we have empirically used the analytical thermal spike model (a-TS) proposed by Szenes (1995) for this extrapolation:

$$\sigma_{am}(T) = \pi a^2(0)[\ln(S_e) - \ln(S_{et})] \text{ for } S_e < 2.7S_{et} \quad (11)$$

$$\sigma_{am}(T) = \frac{\pi a^2(0)}{2.7S_{et}} S_e \text{ for } S_e > 2.7S_{et} \quad (12)$$

$a(0)$ is the width of the Gaussian radial distribution of temperature around the ion track at $t = 0$ (peak temperature). S_{et} is a threshold value of S_e, where no continuous track formation and no amorphization are expected for $S_e < S_{et}$. The parameter a(0), which is directly related to the radius of the trace, is left free and does not prejudge the mechanisms of temperature control of the amorphization kinetics.

Table 2
Parameters obtained by fitting σ_{am} as a function of S_e at temperature T with Eqs. (11) and (12).

T (K)	$a(0)$ (nm)	S_{et} (keV/µm)
90	2.06 ± 0.61	38.8 ± 23.2
100	2.06 ± 0.32	53.8 ± 16.9
110	1.72 ± 0.20	67.9 ± 16.4

We have used these equations to fit the experimental data over an extended range of 10-10^4 keV/µm and determined the $a(0)$ and S_{et} parameters (Table 2). The fits for T=90, 100 and 110 K are presented in Figs. 11 and 5(b). They were obtained from the subset of measurements corresponding to ion fluxes of $5 - 6 \times 10^{10}$ ions/cm^2/s, to prevent from biases of the flux dependence. The shaded area corresponds to the 95% confidence interval. The fit of the experimental data is much better than that obtained with the i-TS model. The parameter a(0) decreases with temperature, in agreement with experimental data.

The quality of the extrapolation of these fits to high S_e values can be discussed in the light of the data of Ding (2014) and Dartois et al. (2015) (Fig. 11). The experimental values reported in Ding (2014) were obtained by irradiating water ice with 19.6 MeV Ne^{6+} at 15 K, 81 MeV Ta^{24+} at 17 K and 46 MeV Ni^{11+} at 145 K. Their data collected at 15 and 17 K are located on our extrapolated cross-section curve at 100 K. The irradiation conducted at 145 K only led to a partial amorphization of water ice due to the fast recrystallization, and consistently to a lower

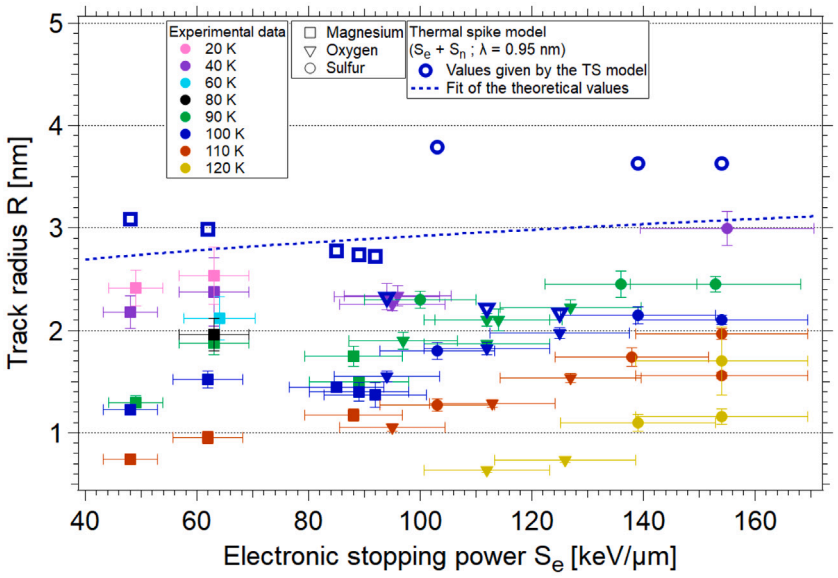

Fig. 10. Experimental track radius as a function of electronic stopping power S_e. Values computed with the i-TS model with the nuclear and electronic regimes are included.

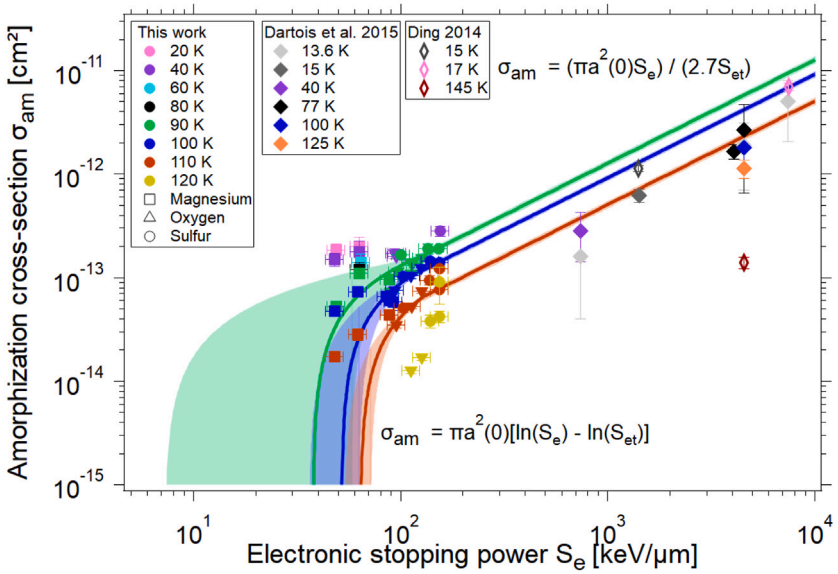

Fig. 11. Amorphization cross-section as a function of electronic stopping power. Extrapolations of the regressions using a-TS model presented in Fig. 5(b) are shown (Eq. (7), (8) and Table 2). Values from this study are compared to those from Ding (2014) and Dartois et al. (2015).

σ_{am} value. In the study by Dartois et al. (2015), water ice was irradiated with high-energy ions between 81 and 3640 MeV over a broad range of temperature (13.6–125 K), resulting in S_e values one to two orders of magnitude higher than those explored in this work. Their value of σ_{am} at 100 K matches our extrapolation based on data collected at 110 K, and is around 2–3 times lower than an estimate from the extrapolation at 100 K. The cross-section at 125 K plots below the extrapolation at 110 K, which is consistent with the temperature dependence. However, the data in the temperature range 13.6–77 K all plot below the 100 K extrapolation, which is inconsistent with the expected temperature trend.

There are three potential explanations for these differences. First, given the high S_e values, the nuclear stopping power is negligible compared to the electronic one in the study of Dartois et al. (2015). However, in our experiments, the S_n values are significant compared to the S_e values (see Table 1). As discussed above, although the cross-section does not correlate with the elastic stopping power S_n, it remains unclear whether it contributes to amorphization. Second, in our study, we used the entire broad OH band from 2900 to 3700 cm^{-1}, to monitor the amorphous fraction during irradiation, fitting each intermediate spectrum with a linear combination of amorphous and crystalline spectra. The study by Dartois et al. (2015) simultaneously investigated the amorphization kinetics and the sputtering yield, which is not negligible with swift heavy ions. They used a narrower region of the OH band from 3000 to 3250 cm^{-1} and the amorphous fraction was determined by fitting the optical depth as a function of fluence using a parametric equation that included the sputtering yield, the fraction of crystalline water, and the band strengths of crystalline and amorphous water ice. The cross-sections obtained by this method then rely on the precise knowledge on the band strengths A_c and A_{am} of crystalline and amorphous water ice, respectively. Third, the irradiation fluxes used in the study by Dartois et al. (2015) may differ from those used in our experiments. Unfortunately, the flux values are not provided in their study.

In conclusion, the parametric equations derived from the a-TS model provide a fair estimate of cross-sections within a factor between 5 to 8, which is not enough to infer the temperature dependency. Extrapolations to low values of Se (< 80 keV/μm) are not constrained by any experimental data. At 90 K the confidence intervals are very large. The cutoff of the extrapolation range must be set to 80 keV/μm.

4. Discussion

Contrary to what has been reported in previous studies, the amorphization cross-section of crystalline water ice bombarded with low-energy ions is not controlled by the total stopping power, nor the nuclear stopping power (Figs. 4(b) and 4(c)). The good linear correlation between the amorphization cross-section and the electronic stopping power (Fig. 4(d)) suggests that the electronic interaction is the main parameter controlling the amorphization mechanism. This finding raises the question of the mechanism responsible for the electronic energy transfer to the lattice of water ice.

In light of the failure of the thermal spike model to interpret the experimental results, there is a need to explore alternative models that describe inelastic interactions.

In the Coulomb explosion model, the ionization along the track promotes repulsive interactions between atoms. In cases where these interactions exceed the strength of atomic bonds, atomic displacements occur, resulting in amorphization. This model has been employed to interpret the sputtering of water ice, with its numerical code developed for liquid water (Costantini and Ogawa, 2023). However, as demonstrated in the study by Teolis et al. (2017), sputtering is confined to a very shallow layer at the uppermost region of the ice crystal (≈ 30 Å).

In the bond weakening model, the weakening of covalent bonds is attributed to ionization, which results in a softer lattice that is more sensitive to collisions or thermal excitation (Van Vechten et al., 1979). This model has been used in the field of semiconductor research, particularly in the context of Si, Ge, and GaAs, to elucidate the mechanisms of annealing processes.

The self-trapped exciton (STE) model posits that an exciton, formed through inelastic interactions, engenders local distortions in the lattice, leading to a reduction in bond strength and, ultimately, its local self-trapping. This process is expected to trigger structural modification or to release heat through non-radiative electron–hole recombination (Itoh, 1996). The STE model has been successfully applied to SiO_2 by fitting the track radius versus the stopping power. Its application to water ice has been restricted to investigating radiolysis and H_2 release, but not to amorphization (Le Caër, 2011).

These three models, Coulomb explosion, bond weakening, and self-trapped excitation, propose alternative explanations for the generation of lattice disorder by inelastic interactions. For water ice, the difference between crystalline and amorphous phase is mostly described in terms of wider distributions of the O–O bond distances and of the bond angles. These variations strongly reduce the position correlations between atoms at medium and long distances, unlike crystalline ice, while mostly preserving its tetrahedral coordination with its first neighbors, as described by neutron diffraction studies of amorphous ice (Chowdhury, 1982). Consequently, amorphous ice is best described as a continuous random network of water molecules with all hydrogen bonds preserved (Boutron and Alben, 1975). The amorphization process thus needs only some relatively weak displacements of the oxygen atoms to distort the correlation with its neighbors and the breaking of O–H and O–O bonds is not necessary. In addition, the presence of other molecules which may be created by radiolysis should create local defects in the H_2O network. These defects should propagate disorder, affecting both interatomic distances and angles over several interatomic distances, thus expanding the regions of amorphized ice.

However, the temperature and flux dependence of the amorphization kinetics remains unaddressed. Energetic particle bombardment of water ice has been shown to cause charge formation and dielectric breakdown (“sparking”), which might possibly cause amorphization (Baragiola et al., 2003; Baragiola et al., 2008; Shi et al., 2012; Jordan, 2022). Noticeably, the probability of dielectric breakdown increases as the temperature decreases and/or as the particle flux increases, as the water ice amorphization cross-section does in our experiments. In the context of swift heavy-ion irradiation of dielectrics, where elastic interactions are absent, an increase in the amorphization kinetics is typically observed as the irradiation temperature is increased. Indeed, an increase in the sample temperature results in a decrease in the energy required to melt the solid within the ion track, as the melting temperature approaches. However, this phenomenon does not occur in water ice that has been exposed to swift heavy ions, where an amorphization efficiency that decreases with increasing temperature is observed (Dartois et al., 2015). Therefore, it is likely that water ice does not melt in ion tracks and that a temperature-dependent recrystallization process competes efficiently with amorphization. The most plausible explanation is that amorphization in water ice is achieved through the generation of defects, which undergo a process of coalescence to form a continuous amorphous irradiation track (Brown et al., 1984). The temperature dependence could be then due to an irradiation-induced recrystallization, as proposed by Wang et al. (2000) in metallic materials. As hypothesized in the previous paragraph, these defects may be due to the radiolysis of H_2O. In the bulk of the sample, the main radiolytic by-product is the moderately abundant H_2O_2 (approximately 1%), due to the rapid recombination of radicals with hydrogen atoms (Loeffler et al., 2006). Notably, an increase in the absorption band of H_2O_2 at approximately 2850 cm^{-1} is observed during irradiation across several spectra presented in Fig. B.1. Although rare, the production of H_2O_2 might be the only remnant of many other transient radiolytic species formed and destroyed within the ice. The rearrangements/displacements of H_2O molecules consecutive to such a radiolytic chemistry might thus explain the observed amorphization. Noticeably, Mejía et al. (2022) have found that H_2O_2 formation and destruction cross-sections in water ice irradiated by swift heavy ions depend linearly with S_e, and they have also found that the H_2O destruction rate is almost 4 times higher at 15 K than at 144 K. These similarities with the dependencies of the water ice amorphization cross-section with the S_e and the temperature, found in the present study, suggest a potential causal link between radiolysis and amorphization. Moreover, this mechanism would be in line with the observation by Leto and Baratta (2003) of the full amorphization of water ice after radiolysis with Lyman-alpha photons.

An intriguing observation is the lack of correlation between the amorphization cross-section and the nuclear stopping power. Indeed, in our experiments, the S_n/S_e ratio varies in the range ~ 0.5–4, which means that the amount of elastic energy is significant. In the context of low-energy ion in the elastic regime, a primary knocked-on atom undergoes a momentum transfer to surrounding atoms, thereby initiating a cascade recoil process. It has been demonstrated that this collisional network generates atomic displacements and a high local density of defects (Sigmund, 1968). This mechanism offers an explanation for the amorphization of implanted silicon when exposed to keV ions, as evidenced by experimental studies (Dennis and Hale, 1978). Another mechanism that involves elastic interactions is the defect-accumulation model. It provides a detailed description of the process by which defects are produced, gradually accumulating along the ion track until ultimately reaching a state of amorphous phase. This transition is marked by reaching a critical defect density threshold (Wang et al., 2000). Amorphization has been observed to occur in experiments above a critical nuclear dose, the magnitude of which increases with temperature (Lian et al., 2005; Lian et al., 2009; Faure et al., 2021). The temperature dependence is interpreted by the interplay between damage production and recovery processes. The origin of the efficient recrystallization, even at temperatures for which no crystallization or molecular agitation are expected over the duration

of an experiment, remains unclear. Wang et al. (2000) proposed that recrystallization associated to a collisional cascade is controlled by diffusion and irradiation-enhanced dynamic annealing. In their model, a crystallization efficiency described by an Arrhenius law is proposed. Such a process would explain why more efficient recrystallization happens at lower temperatures than those required by thermal crystallization over the characteristic time of the experiment (in our case, a couple of hours).

However, a comprehensive understanding of the relative contributions of elastic and inelastic interactions remains elusive. Although the electronic interactions appear to dominate the amorphization process, we cannot fully exclude a contribution of nuclear interactions, in particular if this contribution lies in the form of a critical amorphization dose (Lian et al., 2005; Lian et al., 2009; Faure et al., 2021). In this regard, this contribution may appear in the coefficients of the linear fit of σ_{am} with S_e.

5. Conclusion

The main conclusions of this study are the following:

- Experiments conducted with oxygen, magnesium and sulfur ions at low energy (36–126 keV) show that the water ice amorphization cross-section correlates with the electronic stopping power S_e, and not with the nuclear stopping power S_n nor with total stopping power S. This result invalidates the previous assumption that the total stopping power (i.e. the total dose) controls the water ice amorphization process.
- The water ice amorphization cross-section decreases as the temperature increases from 20 to 120 K.
- A flux dependence of the amorphization cross-section was observed, confirming the earlier results of Golecki and Jaccard (1978). This effect increases with temperature, and is weak below 100 K. Future studies need to assess how these experimental results can be extrapolated to Jovian satellite conditions where expected fluxes are lower by at least 3 orders of magnitude.
- The extrapolation to higher S_e values using the analytical thermal spike model (a-TS) and data from Dartois et al. (2015) and Ding (2014) is not very accurate and does not account for the temperature variations.
- The numerical inelastic thermal spike model (i-TS) was used to analyze experimental data collected over the temperature range 90–120 K. The radius of the ion track R versus electronic stopping power was satisfactorily fit in the case of the pure electronic regime. However, the general trend of a decrease of the cross-section with increasing temperature is not reproduced.
- Alternative models are discussed, addressing the respective contributions of elastic and inelastic interactions. The extent and nature of elastic interactions contribution remain elusive. The amorphization mechanism remains largely unknown.

CRediT authorship contribution statement

A. Moingeon: Writing – original draft, Visualization, Software, Project administration, Data curation. **E. Quirico:** Writing – original draft, Supervision, Project administration, Methodology, Investigation, Data curation. **O. Poch:** Writing – original draft, Supervision, Project administration, Methodology, Investigation, Funding acquisition, Data curation. **M. Faure:** Writing – review & editing, Investigation. **P. Boduch:** Writing – review & editing, Investigation. **A. Domaracka:** Writing – review & editing, Investigation. **H. Rothard:** Writing – review & editing, Investigation. **B. Schmitt:** Writing – review & editing, Investigation. **M. Toulemonde:** Writing – review & editing, Software, Investigation. **J. Rangama:** Writing – review & editing, Software. **D. Bockelée-Morvan:** Writing – review & editing, Funding acquisition. **T. Fouchet:** Writing – review & editing, Funding acquisition. **F. Leblanc:** Writing – review & editing, Funding acquisition. **E. Lellouch:** Writing – review & editing, Funding acquisition. **V. Zakharov:** Writing – review & editing, Funding acquisition.

Declaration of competing interest

The authors declare that they have no known competing financial interests or personal relationships that could have appeared to influence the work reported in this paper.

Acknowledgments

This work was funded by the Centre National d'Etudes Spatiales (CNES) under the MAJIS/JUICE funding program, and by the Agence Nationale de la Recherche (ANR) under the funding program "Préparer l'exploration du système de Jupiter avec JWST" (PRESSE, ANR-21-CE49-0019-02). The experiments were performed at the ARIBE platform of the Grand Accélérateur National d'Ions Lourds (GANIL) by means of the CIRIL Interdisciplinary Platform, part of CIMAP laboratory, Caen, France. We thank the staff of GANIL and CIMAP-CIRIL, in particular Patrick Rousseau and Claire Feierstein, for their invaluable support. We acknowledge the funding from the French National Research Agency, ANR IGLIAS (grant ANR-13-BS05-0004). The authors thank also Lydie Bonal to have uploaded the set of data in the SSHADE database infrastructure. Finally, the authors would like to thank the two anonymous reviewers for their careful reading of the manuscript and for their insightful suggestions, which significantly improved its quality.

Appendix A. Interactions, stopping powers and doses

An ion passing through a solid undergoes two types of interactions. Inelastic interactions of the ion with the electrons of the atoms or molecules lead to ionization, bond weakening or breaking, defects and the formation of a plasma composed of high temperature electrons that transfer their energy to the atomic lattice as heat. These interactions also generate defects in the lattice. The second type of interactions, named nuclear or elastic, is due to interactions between nuclei, generating collision cascades and atomic displacements.

The average amount of energy lost per unit length is defined by the electronic and nuclear stopping powers S_e and S_n in eV/cm, respectively. The total dose deposited per unit of volume, in eV/cm^3, then reads:

$D = D_e + D_n$ with: $D_{e,n} = FS_{e,n}$

where D_e and D_n are the electronic and nuclear doses, respectively, and F is the fluence in ions/cm^2. The total dose, in eV/molecule, is expressed as :

$$D_{e,n} = \frac{M}{\rho N_a} F S_{e,n}$$

where ρ is the density, M the molar mass and N_a the Avogadro number.

The stopping powers of water ice have been calculated with SRIM 2013, with a density of 0.93 g.cm^{-3}.

Appendix B. The OH stretching band across irradiation

During irradiation, the amorphous fraction was monitored using the OH stretching band centered at 3250 cm^{-1}. The evolution of this band is shown in Fig. 2(a) (at 90 K) and in Fig. B.1 (for temperatures ranging from 20 to 120 K). The highest red spectrum, recorded prior to irradiation, correspond to crystalline water ice, as evidenced by the narrow OH band and the presence of three distinct peaks. During the irradiation, the OH band broadens and its amplitude decreases. By the end of irradiation, it remains one broader peak, indicating complete amorphization of the water ice. Notably, the final amorphous spectra in Fig. B.1 show variations in shape across the different temperatures. This suggests the formation of distinct forms of amorphous water ice (Jenniskens et al., 1998). Moreover, a CO_2 contamination band at 2340 cm^{-1} is visible in several irradiation spectra. While CO_2 is inevitable even in a high-vacuum chamber, it does not affect the water ice amorphization process.

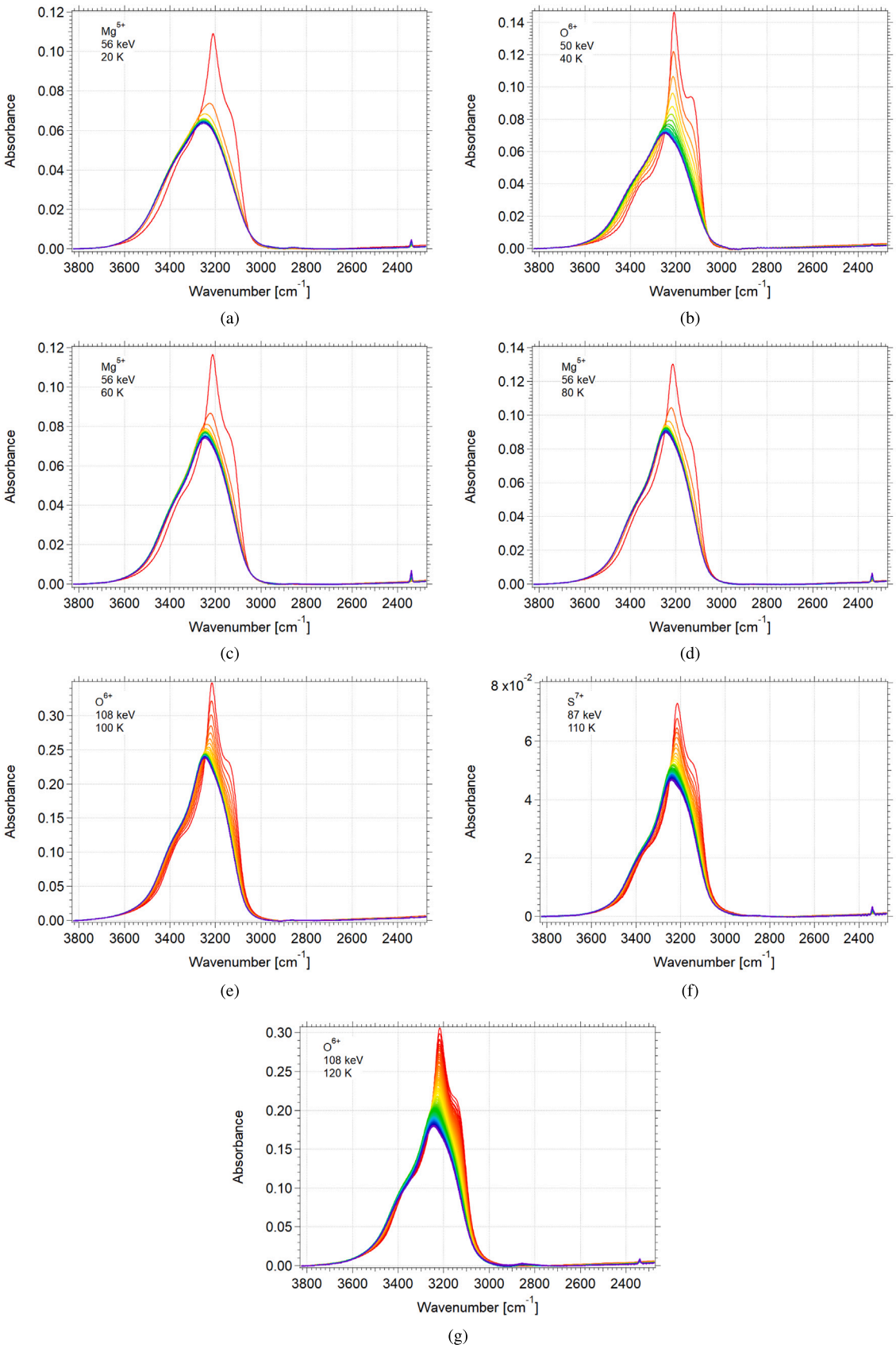

Fig. B.1. Spectra resulting from the irradiation by different ions at temperatures of (a) 20 K, (b) 40 K, (c) 60 K, (d) 80 K, (e) 100 K, (f) 110 K and (g) 120 K. The spectra at 90 K are presented in Fig. 2(a). For each irradiation, the highest red spectrum (crystalline) and the lowest purple spectrum (amorphous) are used to estimate the amorphous fraction in the sample via a linear combination (Eq. (4)). (For interpretation of the references to color in this figure legend, the reader is referred to the web version of this article.)

Data availability

All measured spectra and their associated sample information are freely available through the GhOSST database of the SSHADE infrastructure for solid spectroscopy, supported by the Europlanet 2020-RI program. Direct link to the data is provided in the reference (Moingeon et al., 2024b).

References

Augé, B., Been, T., Boduch, P., Chabot, M., Dartois, E., Madi, T., Ramillon, J.M., Ropars, F., Rothard, H., Voivenel, P., 2018. IGLIAS: A new experimental set-up for low temperature irradiation studies at large irradiation facilities. Rev. Sci. Instrum. 89, 075105. http://dx.doi.org/10.1063/1.5028056.

Awazu, K., Wang, X., Fujimaki, M., Komatsubara, T., Ikeda, T., Ohki, Y., 2006. Structure of latent tracks in rutile single crystal of titanium dioxide induced by swift heavy ions. J. Appl. Phys. 100.

Bar-Nun, A., Herman, G., Rappaport, M.L., Mekler, Y., 1985. Ejection of H2O, O2, H2 and H from water ice by 0.5–6 keV H+ and Ne+ ion bombardment. Surf. Sci. 150, 143–156. http://dx.doi.org/10.1016/0039-6028(85)90215-8, URL: https://www.sciencedirect.com/science/article/pii/0039602885902158.

Baragiola, R.A., Famá, M., Loeffler, M.J., Raut, U., Shi, J., 2008. Radiation effects in ice: New results. Nucl. Instruments Methods Phys. Res. B 266, 3057–3062. http://dx.doi.org/10.1016/j.nimb.2008.03.186.

Baragiola, R.A., Loeffler, M.J., Raut, U., Vidal, R.A., Wilson, C.D., 2005. Laboratory studies of radiation effects in water ice in the outer solar system. Radiat. Phys. Chem. 72, 187–191. http://dx.doi.org/10.1016/j.radphyschem.2004.09.013, URL: https://linkinghub.elsevier.com/retrieve/pii/S0969806X04004955.

Baragiola, R.A., Vidal, R.A., Svendsen, W., Schou, J., Shi, M., Bahr, D.A., Atteberrry, C.L., 2003. Sputtering of water ice. Nucl. Instruments Methods Phys. Res. B Beam Interactions Mater. Atoms 209, 294–303. http://dx.doi.org/10.1016/S0168-583X(02)02052-9, URL: https://www.sciencedirect.com/science/article/pii/S0168583X02020529.

Baratta, G., Leto, G., Spinella, F., Strazzulla, G., Foti, G., 1991. The 3.1 mu.m feature in ion-irradiated water ice. Astron. Astrophys. 252, 421.

Berland, B., Brown, D., Tolbert, M., George, S., 1995. Refractive index and density of vapor-deposited ice. Geophys. Res. Lett. 22, 3493–3496. http://dx.doi.org/10.1029/95GL03504, URL: https://agupubs.onlinelibrary.wiley.com/doi/10.1029/95GL03504.

Bockelée-Morvan, D., Lellouch, E., Poch, O., Quirico, E., Cazaux, S., de Pater, I., Fouchet, T., Fry, P.M., Rodriguez-Ovalle, P., Tosi, F., Wong, M.H., Boshuizen, I., de Kleer, K., Fletcher, L.N., Meunier, L., Mura, A., Roth, L., Saur, J., Schmitt, B., Trumbo, S.K., Brown, M.E., O'Donoghue, J., Orton, G.S., Showalter, M.R., 2024. Composition and thermal properties of Ganymede's surface from JWST/NIRSpec and MIRI observations. Astron. Astrophys. 681, A27. http://dx.doi.org/10.1051/0004-6361/202347326, URL: http://arxiv.org/abs/2310.13982. arXiv:2310.13982 [astro-ph].

Boutron, P., Alben, R., 1975. Structural model for amorphous solid water. J. Chem. Phys. 62, 4848–4853. http://dx.doi.org/10.1063/1.430395, URL: https://pubs.aip.org/jcp/article/62/12/4848/453166/Structural-model-for-amorphous-solid-water.

Brown, M.E., 2016. The 3–4 μm spectra of jupiter trojan asteroids. Astron. J. 152, 159. http://dx.doi.org/10.3847/0004-6256/152/6/159, URL: https://iopscience.iop.org/article/10.3847/0004-6256/152/6/159.

Brown, W., Augustyniak, W., Marcantonio, K., Simmons, E., Boring, J., Johnson, R., Reimann, C., 1984. Electronic sputtering of low temperature molecular solids. Nucl. Instruments Methods Phys. Res. B Beam Interactions Mater. Atoms 1, 307–314. http://dx.doi.org/10.1016/0168-583X(84)90085-5, URL: https://www.sciencedirect.com/science/article/pii/0168583X84900855.

Brown, D.E., George, S.M., Huang, C., Wong, E.K.L., Rider, K.B., Smith, R.S., Kay, B.D., 1996. H_2O condensation coefficient and refractive index for vapor-deposited ice from molecular beam and optical interference measurements. J. Phys. Chem. 100, 4988–4995. http://dx.doi.org/10.1021/jp952547j, URL: https://pubs.acs.org/doi/10.1021/jp952547j.

Chowdhury, M.R., 1982. The Structural Characteristics of Amorphous D20 Ice by Neutron Diffraction.

Costantini, J.-M., Ogawa, T., 2023. Coulomb spike modelling of ion sputtering of amorphous water ice. Quantum Beam Sci. 7, 7. http://dx.doi.org/10.3390/qubs7010007, URL: https://ui.adsabs.harvard.edu/abs/2023QBS.....7....7C. ADS Bibcode: 2023QBS.....7....7C.

Dalton, J.B., Cruikshank, D.P., Stephan, K., McCord, T.B., Coustenis, A., Carlson, R.W., Coradini, A., 2010. Chemical composition of icy satellite surfaces. Space Sci. Rev. 153, 113–154. http://dx.doi.org/10.1007/s11214-010-9665-8, URL: http://link.springer.com/10.1007/s11214-010-9665-8.

Dartois, E., Augé, B., Boduch, P., Brunetto, R., Chabot, M., Domaracka, A., Ding, J.J., Kamalou, O., Lv, X.Y., Rothard, H., Da Silveira, E.F., Thomas, J.C., 2015. Heavy ion irradiation of crystalline water ice: Cosmic ray amorphisation cross-section and sputtering yield. Astron. Astrophys. 576, A125. http://dx.doi.org/10.1051/0004-6361/201425415, URL: http://www.aanda.org/10.1051/0004-6361/201425415.

Davies, J.K., Roush, T.L., Cruikshank, D.P., Bartholomew, M.J., Geballe, T.R., Owen, T., De Bergh, C., 1997. The detection of water ice in comet Hale-Bopp. Icarus 127, 238–245. http://dx.doi.org/10.1006/icar.1996.5673, URL: https://linkinghub.elsevier.com/retrieve/pii/S0019103596956730.

De Barros, A.L.F., Farenzena, L.S., Andrade, D.P.P., Da Silveira, E.F., Wien, K., 2011. Secondary ion emission from water ice at 10–130 K induced by MeV N^{2+} Ions. J. Phys. Chem. C 115, 12005–12014. http://dx.doi.org/10.1021/jp111152y, URL: https://pubs.acs.org/doi/10.1021/jp111152y. Publisher: American Chemical Society (ACS).

Dennis, J.R., Hale, E.B., 1978. Crystalline to amorphous transformation in ion-implanted silicon: A composite model. J. Appl. Phys. 49, 1119–1127. http://dx.doi.org/10.1063/1.325049, URL: https://pubs.aip.org/jap/article/49/3/1119/505304/Crystalline-to-amorphous-transformation-in-ion.

Ding, J.-J., 2014. Irradiation of Water Ice and Astrophysical Implication (Ph.D. thesis). URL: http://www.theses.fr/2014CAEN2056.

Ding, J., Boduch, P., Domaracka, A., Guillous, S., Langlinay, T., Lv, X., Palumbo, M., Rothard, H., Strazzulla, G., 2013. Implantation of multiply charged sulfur ions in water ice. Icarus 226, 860–864. http://dx.doi.org/10.1016/j.icarus.2013.07.002, URL: https://linkinghub.elsevier.com/retrieve/pii/S0019103513003035.

Drechsel-Grau, C., Marx, D., 2014. Quantum simulation of collective proton tunneling in hexagonal ice crystals. Phys. Rev. Lett. 112, 148302. http://dx.doi.org/10.1103/PhysRevLett.112.148302, URL: https://link.aps.org/doi/10.1103/PhysRevLett.112.148302.

Dufour, C., Audouard, A., Beuneu, F., Dural, J., Girard, J., Hairie, A., Levalois, M., Paumier, E., Toulemonde, M., 1993. A high-resistivity phase induced by swift heavy-ion irradiation of Bi: A probe for thermal spike damage? J. Phys.: Condens. Matter. 5, 4573–4584. http://dx.doi.org/10.1088/0953-8984/5/26/027, URL: https://iopscience.iop.org/article/10.1088/0953-8984/5/26/027.

Dufour, C., Beuneu, F., Paumier, E., Toulemonde, M., 1999. Experimental evidence of the irradiation temperature effect in bismuth under swift heavy-ion irradiation. Eur. Lett. 45, 585–590. http://dx.doi.org/10.1209/epl/i1999-00207-5, URL: https://iopscience.iop.org/article/10.1209/epl/i1999-00207-5.

Dufour, C., De Chezelles, B.L., Delignon, V., Toulemonde, M., Paumier, E., Mazzoldi, P., 1992. A transient thermodynamic model for track formation in amorphous semiconductors: A possible mechanism? Chem. Phys. Modif. Induc. Irradiat. Glas. 126, 61.

Dufour, C., Toulemonde, M., 2016. Models for the description of track formation. In: Ion Beam Modification of Solids: Ion-Solid Interaction and Radiation Damage. Springer, pp. 63–104.

Dunlop, A., Lesueur, D., Legrand, P., Dammak, H., Dural, J., 1994. Effects induced by high electronic excitations in pure metals: A detailed study in iron. Nucl. Instruments Methods Phys. Res. B Beam Interactions Mater. Atoms 90, 330–338.

Famá, M., Loeffler, M., Raut, U., Baragiola, R., 2010. Radiation-induced amorphization of crystalline ice. Icarus 207, 314–319. http://dx.doi.org/10.1016/j.icarus.2009.11.001, URL: https://linkinghub.elsevier.com/retrieve/pii/S0019103509004400.

Fatemi, S., Poppe, A.R., Khurana, K.K., Holmström, M., Delory, G.T., 2016. On the formation of Ganymede's surface brightness asymmetries: Kinetic simulations of Ganymede's magnetosphere. Geophys. Res. Lett. 43, 4745–4754. http://dx.doi.org/10.1002/2016GL068363, URL: https://agupubs.onlinelibrary.wiley.com/doi/10.1002/2016GL068363.

Faure, M., Quirico, E., Faure, A., Boduch, P., Rothard, H., Balanzat, E., Baklouti, D., Brunetto, R., Bonal, L., Beck, P., Schmitt, B., 2021. A radiolytic origin of organic matter in primitive chondrites and trans-neptunian objects? New clues from ion irradiation experiments. Icarus 364, 114462. http://dx.doi.org/10.1016/j.icarus.2021.114462, URL: https://linkinghub.elsevier.com/retrieve/pii/S0019103521001445.

Franks, F., 1972. The properties of ice. In: The Physics and Physical Chemistry of Water. Springer, pp. 115–149.

Golecki, I., Jaccard, C., 1978. Radiation damage in ice at low temperatures studied by proton channelling. J. Glaciol. 21, 247–258. http://dx.doi.org/10.1017/S0022143000033451.

Handa, Y.P., Klug, D.D., 1988. Heat capacity and glass transition behavior of amorphous ice. J. Phys. Chem. 92, 3323–3325. http://dx.doi.org/10.1021/j100323a005, URL: https://pubs.acs.org/doi/abs/10.1021/j100323a005.

Hansen, G.B., McCord, T.B., 2004. Amorphous and crystalline ice on the Galilean satellites: A balance between thermal and radiolytic processes. J. Geophys. Res. Planets 109, 2003JE002149. http://dx.doi.org/10.1029/2003JE002149, URL: https://agupubs.onlinelibrary.wiley.com/doi/10.1029/2003JE002149.

Heide, H.-G., 1984. Observations on ice layers. Ultramicroscopy 14, 271–278. http://dx.doi.org/10.1016/0304-3991(84)90095-0, URL: https://linkinghub.elsevier.com/retrieve/pii/0304399184900950.

Hermes, P., Danielzik, B., Fabricius, N., Linde, D., Kuhl, J., Heppner, J., Stritzker, B., Pospieszczyk, A., 1986. Evaporation of atoms from femtosecond laser-heated gallium arsenide. Appl. Phys. A Solids Surfaces 39, 9–11. http://dx.doi.org/10.1007/BF01177158, URL: http://link.springer.com/10.1007/BF01177158.

Hollis, M.J., 1973. Channeling of 1-MeV he$^+$ ions in NaCl: Damage and temperature effects. Phys. Rev. B 8, 931–935. http://dx.doi.org/10.1103/PhysRevB.8.931.

Houpert, C., Studer, F., Pascard, H., YunFan, J., Toulemonde, M., 1991. Influence of the substrate temperature on the latent track damage cross section in magnetic insulators. Int. J. Radiat. Appl. Instrum. Nucl. Tracks Radiat. Meas. 19, 85–90. http://dx.doi.org/10.1016/1359-0189(91)90147-A, URL: https://linkinghub.elsevier.com/retrieve/pii/135901899190147A.

Hudson, R.L., Palumbo, M.E., Strazzulla, G., Moore, M.H., Cooper, J.F., Sturner, S.J., 2008. Laboratory Studies of the Chemistry of Transneptunian Object Surface Materials.

Itoh, N., 1996. Self-trapped exciton model of heavy-ion track registration. Nucl. Instruments Methods Phys. Res. B 116, 33–36. http://dx.doi.org/10.1016/0168-583X(96)00006-7.

Jenniskens, P., Blake, D.F., Kouchi, A., 1998. Amorphous water ice. In: Schmitt, B., De Bergh, C., Festou, M. (Eds.), Solar System Ices. In: Astrophysics and Space Science Library, vol. 227, Springer Netherlands, Dordrecht, pp. 139–155. http://dx.doi.org/10.1007/978-94-011-5252-5_7, URL: http://link.springer.com/10.1007/978-94-011-5252-5_7.

Jordan, A., 2022. Reevaluating how charged particles cause space weathering on airless bodies. Icarus 376, 114878. http://dx.doi.org/10.1016/j.icarus.2021.114878.

Kim, S., Sattorov, M., Hong, D., Kang, H., Park, J., Lee, J.H., Ma, R., Martin, A.V., Caleman, C., Sellberg, J.A., et al., 2023. Observing ice structure of micron-sized vapor-deposited ice with an x-ray free-electron laser. Struct. Dyn. 10.

Kivelson, M., Khurana, K., Russell, C., Walker, R., Warnecke, J., Coroniti, F., Polanskey, C., Southwood, D., Schubert, G., 1996. Discovery of ganymede's magnetic field by the Galileo spacecraft. Nature 384, 537–541.

Klaumünzer, S., 2006. Thermal-Spike Models for Ion Track Physics: A Critical Examination.

Klinger, J., 1980. Influence of a phase transition of ice on the heat and mass balance of comets. Science 209, 271–272, URL: https://www.jstor.org/stable/1684924, Publisher: American Association for the Advancement of Science.

Le Caër, S., 2011. Water radiolysis: Influence of oxide surfaces on H2 production under ionizing radiation. Water 3, 235–253. http://dx.doi.org/10.3390/w3010235, URL: https://www.mdpi.com/2073-4441/3/1/235.

Lepault, J., Freeman, R., Dubochet, J., 1983. Electron beam induced "vitrified ice". J. Microsc. 132, http://dx.doi.org/10.1111/j.1365-2818.1983.tb04590.x, URL: https://onlinelibrary.wiley.com/doi/10.1111/j.1365-2818.1983.tb04590.x.

Leto, G., Baratta, G.A., 2003. Ly-α photon induced amorphization of Ic water ice at 16 Kelvin: Effects and quantitative comparison with ion irradiation. Astron. Astrophys. 397, 7–13. http://dx.doi.org/10.1051/0004-6361:20021473, URL: http://www.aanda.org/10.1051/0004-6361:20021473.

Leto, G., Gomis, O., Strazzulla, G., 2005. The reflectance spectrum of water ice: Is the 1.65 mu msp peak a good temperature probe? Mem. Della Soc. Astron. Ital. Suppl. 6, 57.

Lian, J., Wang, L., Ewing, R.C., Yudintsev, S.V., Stefanovsky, S.V., 2005. Ion-beam-induced amorphization and order-disorder transition in the muratatite structure. J. Appl. Phys. 97, 113536–113538. http://dx.doi.org/10.1063/1.1926394.

Lian, J., Wang, L., Sun, K., Ewing, R.C., 2009. In situ TEM of radiation effects in complex ceramics. Microsc. Res. Tech. 72, 165–181. http://dx.doi.org/10.1002/jemt.20669.

Ligier, N., Paranicas, C., Carter, J., Poulet, F., Calvin, W., Nordheim, T., Snodgrass, C., Ferellec, L., 2019. Surface composition and properties of Ganymede: Updates from ground-based observations with the near-infrared imaging spectrometer SINFONI/VLT/ESO. Icarus 333, 496–515. http://dx.doi.org/10.1016/j.icarus.2019.06.013, URL: https://linkinghub.elsevier.com/retrieve/pii/S0019103519300053.

Ligier, N., Poulet, F., Carter, J., Brunetto, R., Gourgeot, F., 2016. VLT/SINFONI observations of Europa: New insights into the surface composition. Astron. J. 151, 163.

Liuzzo, L., Poppe, A.R., Paranicas, C., Nénon, Q., Fatemi, S., Simon, S., 2020. Variability in the energetic electron bombardment of Ganymede. J. Geophys. Res. Space Phys. 125, e2020JA028347. http://dx.doi.org/10.1029/2020JA028347, URL: https://onlinelibrary.wiley.com/doi/abs/10.1029/2020JA028347. _eprint: https://onlinelibrary.wiley.com/doi/pdf/10.1029/2020JA028347.

Loeffler, M., Hudson, R., Moore, M., Carlson, R., 2011. Radiolysis of sulfuric acid, sulfuric acid monohydrate, and sulfuric acid tetrahydrate and its relevance to Europa. Icarus 215, 370–380. http://dx.doi.org/10.1016/j.icarus.2011.06.008, URL: https://linkinghub.elsevier.com/retrieve/pii/S001910351100217X.

Loeffler, M., Raut, U., Vidal, R., Baragiola, R., Carlson, R., 2006. Synthesis of hydrogen peroxide in water ice by ion irradiation. Icarus 180, 265–273. http://dx.doi.org/10.1016/j.icarus.2005.08.001, URL: https://linkinghub.elsevier.com/retrieve/pii/S0019103505002848.

Loeffler, M.J., Tribbett, P.D., Cooper, J.F., Sturner, S.J., 2020. A possible explanation for the presence of crystalline H2O-ice on Kuiper belt objects. Icarus 351, 113943. http://dx.doi.org/10.1016/j.icarus.2020.113943, URL: https://linkinghub.elsevier.com/retrieve/pii/S0019103520303171.

Lv, X., De Barros, A., Boduch, P., Bordalo, V., Da Silveira, E., Domaracka, A., Fulvio, D., Hunniford, C., Langlinay, T., Mason, N., McCullough, R., Palumbo, M., Pilling, S., Rothard, H., Strazzulla, G., 2012. Implantation of multiply charged carbon ions in water ice. Astron. Astrophys. 546, A81. http://dx.doi.org/10.1051/0004-6361/201219886, URL: http://www.aanda.org/10.1051/0004-6361/201219886.

Martinez, R., Agnihotri, A., Boduch, P., Domaracka, A., Fulvio, D., Muniz, G., Palumbo, M., Rothard, H., Strazzulla, G., 2019. Production of hydronium ion $(H_3O)^+$ and protonated water clusters $(H_2O)_nH^+$ after energetic ion bombardment of water ice in astrophysical environments. J. Phys. Chem. A 123, 8001–8008. http://dx.doi.org/10.1021/acs.jpca.9b05029, URL: https://pubs.acs.org/doi/10.1021/acs.jpca.9b05029. Publisher: American Chemical Society (ACS).

Mastrapa, R., Sandford, S., Roush, T., Cruikshank, D., Dalle Ore, C., 2009. Optical constants of amorphous and crystalline H_2O-ice: 2.5-22 μm (4000-455 cm^{-1}) optical constants of H_2O-ice. Astrophys. J. 701, 1347–1356. http://dx.doi.org/10.1088/0004-637X/701/2/1347.

Meftah, A., Costantini, J., Khalfaoui, N., Boudjadar, S., Stoquert, J., Studer, F., Toulemonde, M., 2005. Experimental determination of track cross-section in Gd3Ga5O12 and comparison to the inelastic thermal spike model applied to several materials. Nucl. Instrum. Methods Phys. Res. Beam Interactions Mater. Atoms 237, 563–574.

Mejía, C., de Barros, A., Rothard, H., Boduch, P., da Silveira, E., 2022. Swift heavy ions irradiation of water ice at different temperatures: Hydrogen peroxide and ozone synthesis and sputtering yield. Mon. Not. R. Astron. Soc. 514, 3789–3801. http://dx.doi.org/10.1093/mnras/stac1489, URL: https://doi.org/10.1093/mnras/stac1489.

Mélot, M., Ngono-Ravache, Y., Balanzat, E., 2003. Role of the irradiation temperature on the modifications of swift-heavy-ion irradiated polyethylene. Nucl. Instruments Methods Phys. Res. B Beam Interactions Mater. Atoms 209, 205–211. http://dx.doi.org/10.1016/S0168-583X(03)01101-7, URL: https://linkinghub.elsevier.com/retrieve/pii/S0168583X03011017.

Moingeon, A., Quirico, E., Poch, O., Boduch, P., Domaracka, A., Rothard, H., 2024a. MIR spectra of a thin film of water ice at temperature from 50 K to 160 K. http://dx.doi.org/10.26302/SSHADE/EXPERIMENT_LB_20251218_001, SSHADE/GhoSST (OSUG Data Center). Dataset/Spectral Data.

Moingeon, A., Quirico, E., Poch, O., Faure, M., Boduch, P., Domaracka, A., Rothard, H., 2024b. MIR spectra collected before and after irradiation experiments (with different ions at varying energy) of crystalline water ice at temperature from 20 K to 120 K. http://dx.doi.org/10.26302/SSHADE/EXPERIMENT_LB_20250630_001, SSHADE/GhoSST (OSUG Data Center). Dataset/Spectral Data.

Moore, M., Hudson, R., Carlson, R., 2007. The radiolysis of SO2 and H2S in water ice: Implications for the icy jovian satellites. Icarus 189, 409–423. http://dx.doi.org/10.1016/j.icarus.2007.01.018, URL: https://linkinghub.elsevier.com/retrieve/pii/S0019103507000589.

Orton, G., Spencer, J., Travis, L., Martin, T., Tamppari, L., 1996. Galileo photopolarimeter-radiometer observations of jupiter and the Galilean satellites. Science 274, 389–391. http://dx.doi.org/10.1126/science.274.5286.389, URL: https://www.science.org/doi/10.1126/science.274.5286.389.

Paranicas, C., Mauk, B., Kollmann, P., Clark, G., Haggerty, D., Westlake, J., Liuzzo, L., Masters, A., Cassidy, T.A., Bagenal, F., Bolton, S., 2022. Energetic charged particle fluxes relevant to Ganymede's polar region. Geophys. Res. Lett. 49, e2022GL098077. http://dx.doi.org/10.1029/2022GL098077, URL: https://agupubs.onlinelibrary.wiley.com/doi/10.1029/2022GL098077.

Plainaki, C., Massetti, S., Jia, X., Mura, A., Milillo, A., Grassi, D., Sindoni, G., D'Aversa, E., Filacchione, G., 2020. Kinetic simulations of the Jovian energetic ion circulation around Ganymede. Astrophys. J. 900, 74. http://dx.doi.org/10.3847/1538-4357/aba94c, URL: https://ui.adsabs.harvard.edu/abs/2020ApJ...900...74P. ADS Bibcode: 2020ApJ...900...74P.

Poppe, A., Fatemi, S., Khurana, K., 2018. Thermal and energetic ion dynamics in Ganymede's magnetosphere. J. Geophys. Res. Space Phys. 123, 4614–4637. http://dx.doi.org/10.1029/2018JA025312, URL: https://onlinelibrary.wiley.com/doi/abs/10.1029/2018JA025312, _eprint: https://onlinelibrary.wiley.com/doi/pdf/10.1029/2018JA025312.

Rethfeld, B., Sokolowski-Tinten, K., Von Der Linde, D., Anisimov, S., 2002. Ultrafast thermal melting of laser-excited solids by homogeneous nucleation. Phys. Rev. B 65, 092103. http://dx.doi.org/10.1103/PhysRevB.65.092103, URL: https://link.aps.org/doi/10.1103/PhysRevB.65.092103.

Rothard, H., Domaracka, A., Boduch, P., Palumbo, M.E., Strazzulla, G., Da Silveira, E.F., Dartois, E., 2017. Modification of ices by cosmic rays and solar wind. J. Phys. B: At. Mol. Opt. Phys. 50, 062001. http://dx.doi.org/10.1088/1361-6455/50/6/062001, URL: https://iopscience.iop.org/article/10.1088/1361-6455/50/6/062001.

Sall, M., Monnet, I., Moisy, F., Grygiel, C., Jublot-Leclerc, S., Della-Negra, S., Toulemonde, M., Balanzat, E., 2015. Track formation in III-N semiconductors irradiated by swift heavy ions and fullerene and re-evaluation of the inelastic thermal spike model. J. Mater. Sci. 50, 5214–5227.

Salzmann, C.G., Radaelli, P.G., Slater, B., Finney, J.L., 2011. The polymorphism of ice: Five unresolved questions. Phys. Chem. Chem. Phys. 13, 18468. http://dx.doi.org/10.1039/c1cp21712g, URL: https://xlink.rsc.org/?DOI=c1cp21712g. Publisher: Royal Society of Chemistry (RSC).

Schnohr, C., Kluth, P., Giulian, R., Llewellyn, D., Byrne, A., Cookson, D., Ridgway, M.C., 2010. Swift-heavy-ion-induced damage formation in III-V binary and ternary semiconductors. Phys. Rev. B Condensed Matter Mater. Phys. 81, 075201.

Shi, J., Famá, M., Teolis, B., Baragiola, R., 2012. Ion-induced electrostatic charging of ice at 15-160 K. Phys. Rev. B 85, 035424. http://dx.doi.org/10.1103/PhysRevB.85.035424.

Shilling, J., Tolbert, M., Toon, O., Jensen, E., Murray, B., Bertram, A., 2006. Measurements of the vapor pressure of cubic ice and their implications for atmospheric ice clouds. Geophys. Res. Lett. 33, L17801. http://dx.doi.org/10.1029/2006GL026671.

Sigmund, P., 1968. Sputtering efficiency of amorphous substances. Can. J. Phys. 46, 731–737. http://dx.doi.org/10.1139/p68-090.

Strazzulla, G., Baratta, G., Leto, G., Foti, G., 1992. Ion-beam-induced amorphization of crystalline water ice. Eur. Lett. 18, 517–522. http://dx.doi.org/10.1209/0295-5075/18/6/008, URL: https://iopscience.iop.org/article/10.1209/0295-5075/18/6/008.

Szenes, G., 1995. General features of latent track formation in magnetic insulators irradiated with swift heavy ions. Phys. Rev. B 51, 8026–8029. http://dx.doi.org/10.1103/PhysRevB.51.8026, URL: https://link.aps.org/doi/10.1103/PhysRevB.51.8026.

Tegler, S.C., Grundy, W., Loeffler, M., Tribbett, P., Hanley, J., Jasko, A., Dawson, H., Morgan, A., Koga, K., Madden-Watson, A., Gomez, M., Steckloff, J., Lindberg, G., Tan, S., Raposa, S., Engle, A., Thieberger, C., Trilling, D., 2024. Optical constants of ices important to planetary science from laboratory reflectance spectroscopy. Planet. Sci. J. 5, 31. http://dx.doi.org/10.3847/PSJ/ad1683, URL: https://iopscience.iop.org/article/10.3847/PSJ/ad1683.

Teolis, B., Plainaki, C., Cassidy, T., Raut, U., 2017. Water ice radiolytic O_2, H_2, and H_2O_2 yields for any projectile species, energy, or temperature: A model for icy astrophysical bodies. J. Geophys. Res. Planets 122, 1996–2012. http://dx.doi.org/10.1002/2017JE005285, URL: https://agupubs.onlinelibrary.wiley.com/doi/10.1002/2017JE005285.

Terai, T., Itoh, Y., Oasa, Y., Furusho, R., Watanabe, J., 2016. Photometric measurements of H2O ice crystallinity on trans-neptunian objects. Astrophys. J. 827, 65.

Toulemonde, M., Dufour, C., Meftah, A., Paumier, E., 2000. Transient thermal processes in heavy ion irradiation of crystalline inorganic insulators. Nucl. Instruments Methods Phys. Res. Sect. B Beam Interactions Mater. Atoms 166, 903–912.

Toulemonde, M., Dufour, C., Paumier, E., 1992. Transient thermal process after a high-energy heavy-ion irradiation of amorphous metals and semiconductors. Phys. Rev. B 46, 14362–14369. http://dx.doi.org/10.1103/PhysRevB.46.14362, URL: https://link.aps.org/doi/10.1103/PhysRevB.46.14362. Publisher: American Physical Society.

Toulemonde, M., Surdutovich, E., Solov'yov, A.V., 2009. Temperature and pressure spikes in ion-beam cancer therapy. Phys. Rev. E 80, 031913. http://dx.doi.org/10.1103/PhysRevE.80.031913, URL: https://link.aps.org/doi/10.1103/PhysRevE.80.031913.

Van Vechten, J., Tsu, R., Saris, F., Hoonhout, D., 1979. Reasons to believe pulsed laser annealing of Si does not involve simple thermal melting. Phys. Lett. A 74, 417–421. http://dx.doi.org/10.1016/0375-9601(79)90241-X.

Vorburger, A., Fatemi, S., Galli, A., Liuzzo, L., Poppe, A.R., Wurz, P., 2022. 3D Monte-Carlo simulation of Ganymede's water exosphere. Icarus 375, 114810. http://dx.doi.org/10.1016/j.icarus.2021.114810, URL: https://linkinghub.elsevier.com/retrieve/pii/S0019103521004565.

Wang, Z., Dufour, C., Paumier, E., Toulemonde, M., 1994. The Se sensitivity of metals under swift-heavy-ion irradiation: A transient thermal process. J. Phys.: Condens. Matter. 6, 6733.

Wang, S., Wang, L., Ewing, R., 2000. Irradiation-induced amorphization: Effects of temperature, ion mass, cascade size, and dose rate. Phys. Rev. B 63, 024105. http://dx.doi.org/10.1103/PhysRevB.63.024105.

Weber, W.J., Wendler, E., 2016. Modelling effects of radiation damage. Ion Beam Modif. Solids Ion-Solid Interact. Radiat. Damage 105–136.

Whalley, E., 1977. A detailed assignment of the O–H stretching bands of ice I. Can. J. Chem. 55, 3429–3441. http://dx.doi.org/10.1139/v77-481, URL: https://cdnsciencepub.com/doi/10.1139/v77-481.

Zhang, Y., Weber, W.J., 2020. Ion irradiation and modification: The role of coupled electronic and nuclear energy dissipation and subsequent nonequilibrium processes in materials. Appl. Phys. Rev. 7, 041307. http://dx.doi.org/10.1063/5.0027462, URL: https://pubs.aip.org/aip/apr/article/832255.

Ziegler, J.F., Ziegler, M., Biersack, J., 2010. SRIM — The stopping and range of ions in matter (2010). Nucl. Instruments Methods Phys. Res. B Beam Interactions Mater. Atoms 268, 1818–1823. http://dx.doi.org/10.1016/j.nimb.2010.02.091, URL: https://linkinghub.elsevier.com/retrieve/pii/S0168583X10001862.